Shock Formation in Overexpanded Flow-
A Study Using the Hydraulic Analogy

by

Kevin M. Elward

Thesis submitted to the Faculty of the
Virginia Polytechnic Institute and State University
in partial fulfillment of the requirements for the degree of
Master of Science
in
Mechanical Engineering

APPROVED:

Dr. John Moore, Chairman

Dr. Thomas E. Diller

Dr. Hal L. Moses

April 1989

Blacksburg, Virginia

Shock Formation in Overexpanded Flow-

A Study Using the Hydraulic Analogy

by

Kevin M. Elward

Dr. John Moore, Chairman

Mechanical Engineering

(ABSTRACT)

Tests were performed to study the mechanism of shock formation in supersonic flow in long orifices to gain insight into the leakage flow of turbine tip gaps. The flow was modeled on a water table using a sharp-edged rectangular channel. The hydraulic analogy between free surface water flows and compressible gas flows was used to study the implications of the water table flow on tip leakage flows.

The flow on the water table exhibited oblique hydraulic jumps starting on the channel sidewall near the channel entrance. This flow was analyzed using the oblique hydraulic jump relations developed by classical hydraulic theory. The results of this analysis suggested a model for the formation of the jump. As the flow accelerates around the corner of the channel entrance, supercritical free stream flow is turned as it intersects the sidewall. The abrupt change in flow direction results in the formation of the oblique hydraulic jump.

An acceptable hydraulic analogy of compressible gas flows with shocks was obtained by reducing the surface tension of the water and using a large model size. The modified analogy for non-isentropic flow then allowed quantitative evaluation of the modeled shock structure in a compressible flow field. The predicted shock formation

in such a flow has possible implications for both the efficiency of a gas turbine and the useful life of the turbine blade.

Acknowledgements

I would like to thank those who participated in the preparation and review of this thesis. First, to Dr. John Moore whose guidance and assistance throughout this project were invaluable to its completion. His ideas and suggestions were always thought-provoking and helpful. Thanks to whose plotting routine was used to prepare the contour plots which appear here. Thanks also to Dr. Thomas Diller and Dr. Hal Moses for serving on my advisory committee and for reviewing this thesis.

I would like to express my gratitude to Rolls-Royce plc, Aero Division, for their support of this project.

I would also like to recognize the many friends here in Blacksburg and elsewhere with whom time spent camping, golfing, playing volleyball, etc. was always a welcome and refreshing retreat from study and research.

Finally, I would especially like to thank my family: my parents and my sisters and brothers-- , , , , and --whose love, support and encouragement made this undertaking possible.

Table of Contents

List of Illustrations

List of Tables

Nomenclature

c	velocity of sound
C_p	constant pressure specific heat
$\frac{\partial}{\partial x}$	partial derivative with respect to x
$\frac{\partial}{\partial y}$	partial derivative with respect to y
F	Froude number
g	acceleration due to gravity
h	tip gap height or water depth
H	enthalpy
k	ratio of specific heats $\frac{C_p}{C_v}$
l	length
M	Mach number
P	static pressure
r	radius
R	ideal gas constant
Re	Reynolds number
T	temperature or surface tension
u	x-direction velocity component
v	y-direction velocity component
V	velocity
w	water channel half-width
x_i	distance from orifice edge to the point of intersection of the free streamline with the orifice wall

Greek letters

β	oblique hydraulic jump angle

δ	deflection or turning angle
λ	wavelength of water wave
ρ	density
σ	oblique shock angle

Subscripts

b	back or downstream conditions
i	intersection point
max	maximum
n	normal direction
t	tangential direction
0	total or upstream conditions
1	conditions upstream of shock or hydraulic jump
2	conditions downstream of shock or hydraulic jump

Chapter I

Introduction

In order to reduce the cost of operation and maintenance, efforts have been made to increase the efficiency and life of turbomachines. The first step in improving efficiency is to identify the sources of loss. One such area which has been the focus of recent research is turbine tip clearance gap leakage. Tip gap leakage arises from the escape of high energy gas from the pressure side of the turbine blade to the suction side through the blade tip clearance gap. Estimates are that tip gap leakage may cause 5% of turbine inefficiencies.

Most of the research on tip gap leakage has been with incompressible flows, focusing mainly on flow visualizations. The relatively little compressible flow research has suggested that shocks may be present in the tip gap. Specifically, overexpansion of the flow around the sharp corner of the blade tip may result in a shock.

Understanding the mechanism of this flow is important not only because of the obvious associated losses, but also because the flow affects the blade heat transfer.

High heat transfer at the blade tip can lead to blade tip rounding which will result in a larger tip clearance gap. A larger tip gap means higher losses of kinetic energy. Eventually, the useful life of the blade will become exhausted. Thus, with an understanding of tip gap flow, problems of inefficiency and life can be addressed.

This investigation will study the mechanism of the shock formation in the tip gap. Using the hydraulic analogy between free surface water flows and compressible gas flows, observations about tip gap flows will be inferred from a study of flow through a rectangular channel on a water table.

Chapter II

Literature Review

Tip Leakage Flow

Although flow through blade tip gaps is important in both the life and efficiency of a turbomachine, relatively little information on this subject can be found in the literature.

Rains [1] presented both an idealized model and a somewhat more realistic model for flow through a compressor blade tip gap. Both models assume the tip gap flow is normal to the blade chamber line. This was done because the pressure gradient across the blade is much greater than that along the blade.

In the idealized model, based on incompressible potential flow theory, the flow has a contraction ratio σ of $\frac{\pi}{\pi + 2} = 0.611$. Rains applied the Bernoulli equation through the tip gap, noting that the pressure along the free streamline is equal to P_2 . This flow is pictured in Fig. 1. No experimental verification was given for this model.

Figure 2 shows Rains' more realistic flow model. In this model, a vena contracta occurs at the tip gap inlet followed by mixing.

Moore and Tilton [2] performed an experimental investigation on tip leakage in a linear turbine blade cascade. From measured static pressures, they were able to infer the existence of a vena contracta in the tip gap inlet. A contraction coefficient of 0.61 was calculated from the data. Following the vena contracta, a region of mixing occurred resulting in a reasonably uniform static pressure across the tip gap exit.

Other experimental investigations on incompressible tip gap flow have been performed by Graham [3] and Bindon [4]. Graham's work involved the measurement of velocity profiles at the tip gap exit, while Bindon focused primarily on examining tip gap flow development.

Graham conducted his research with a water turbine cascade. He varied the Reynolds number for the flow by varying the tip gap height. The resulting velocity profiles for three different Reynolds numbers are shown in Fig. 3, plotted against the corresponding tip gap length given in tip gap heights. The velocity profiles show reattached flows with jets covering 60 to 70 percent of the tip gap.

Bindon's experiments were performed in a linear turbine cascade. Using fine smoke injection into the tip gap, photographs of the flow pattern were taken. Sketches of some of these photographs are shown in Fig. 4. For low Reynolds number flow, the flow shows no sign of separation. At higher Reynolds numbers, however, separation

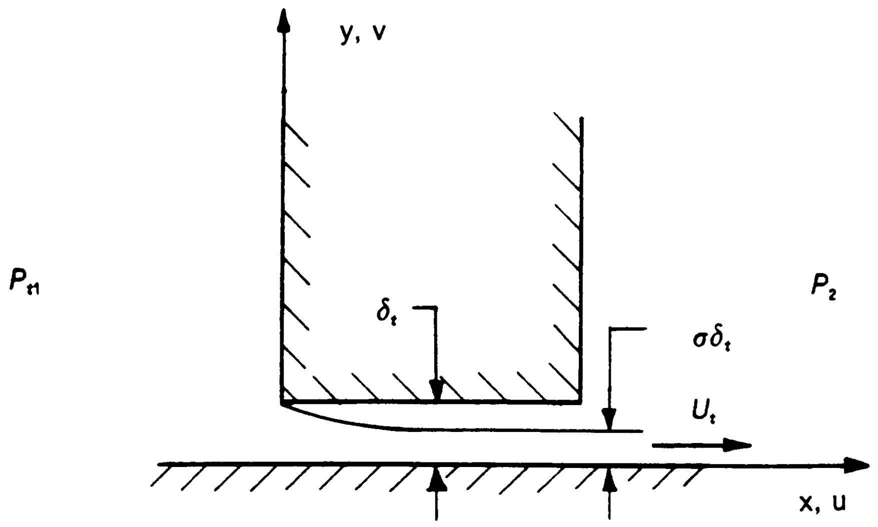

Figure 1. Rains' idealized tip gap flow.

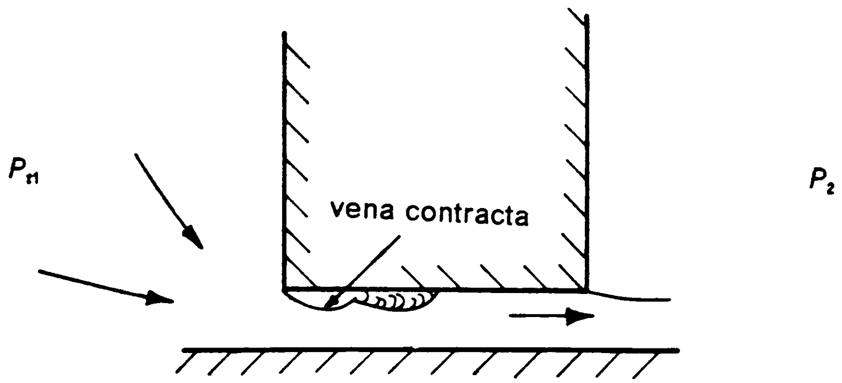

Figure 2. Rains' actual tip gap flow

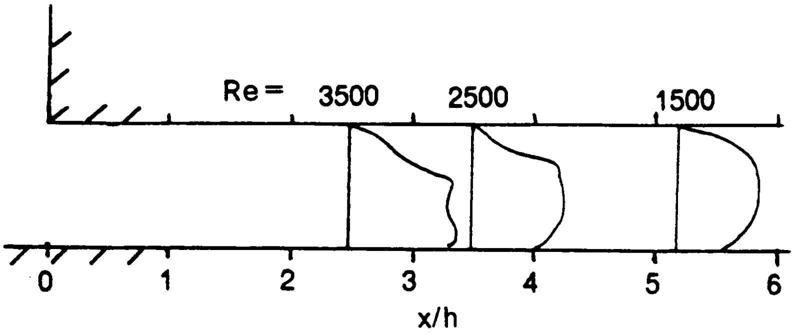

Figure 3. Graham's measured velocity profiles

is seen occurring at about $x/h=2$ with flow in the separation bubble moving along the blade chordwise.

Moore, et al. [5] performed laminar flow calculations for a 2-D tip gap geometry for various Reynolds numbers. Figure 5 plots the calculated velocity vectors for two such cases. The low Reynolds number case ($Re=110$) shows a rapidly developing parabolic velocity profile. Note that unlike Rains' model, there is no separation. In contrast, in the higher Reynolds number case ($Re=1100$), a significant separation region develops with no reattachment within the tip gap. Calculations show reattachment at $x/h=7$ downstream.

Figure 6 shows the calculated velocity profiles for $Re=1100$, with Graham's measured profiles repeated for comparison. While the two show only a qualitative similarity, it must be remembered that the calculations were done for laminar flow. This would suggest the need for turbulence to be included in the calculation, as suggested by Moore and Tilton's results. While the above studies have contributed to the understanding of tip gap flow regimes in general, all have been done on incompressible flows.

Henry [6] studied the compressible effects of tip gap flow by examining compressible flows in orifices. Included in this study was a compressible flow visualization using the hydraulic analogy between free surface water flows and compressible gas flows. While Graham's study was done in a water cascade, it was not a free surface flow study and therefore did not model compressible effects.

Henry performed his flow visualization on a water table. The channel had a length to width ratio of 3.65, modeling a tip gap of length to height ratio of 7.3 and its mirror

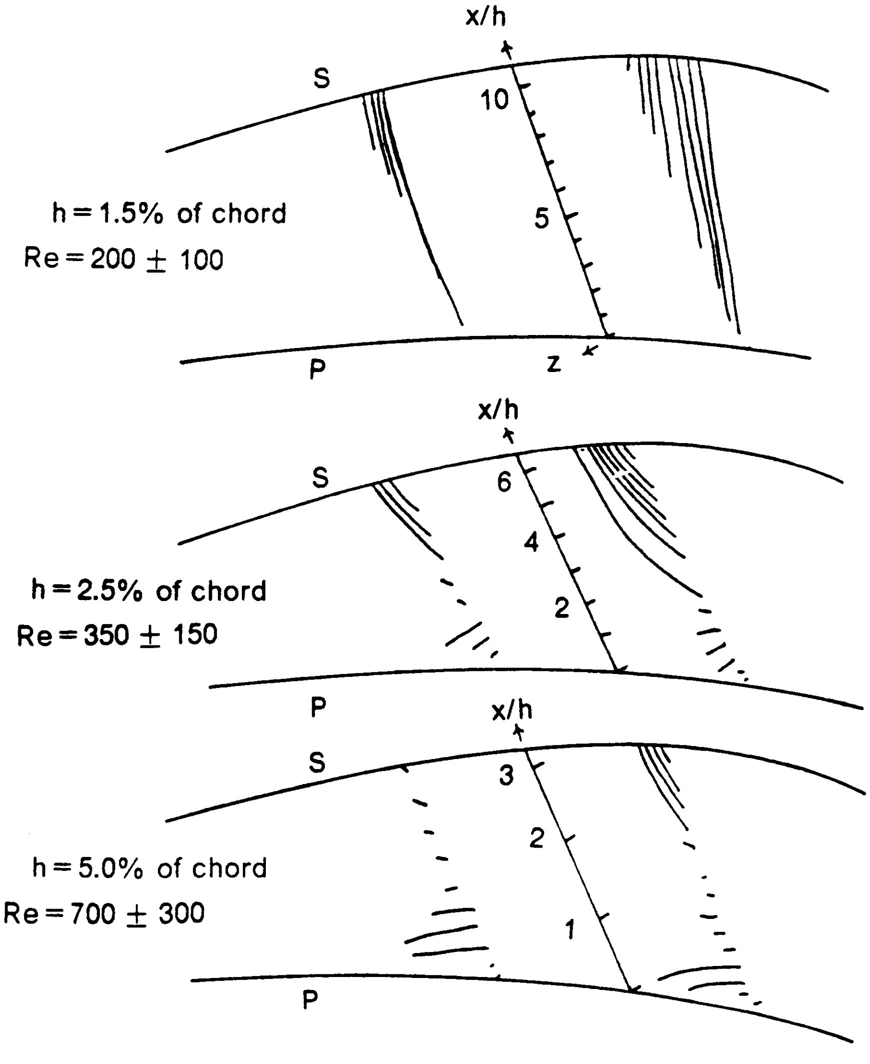

Figure 4. Sketch of Bindon's flow visualization

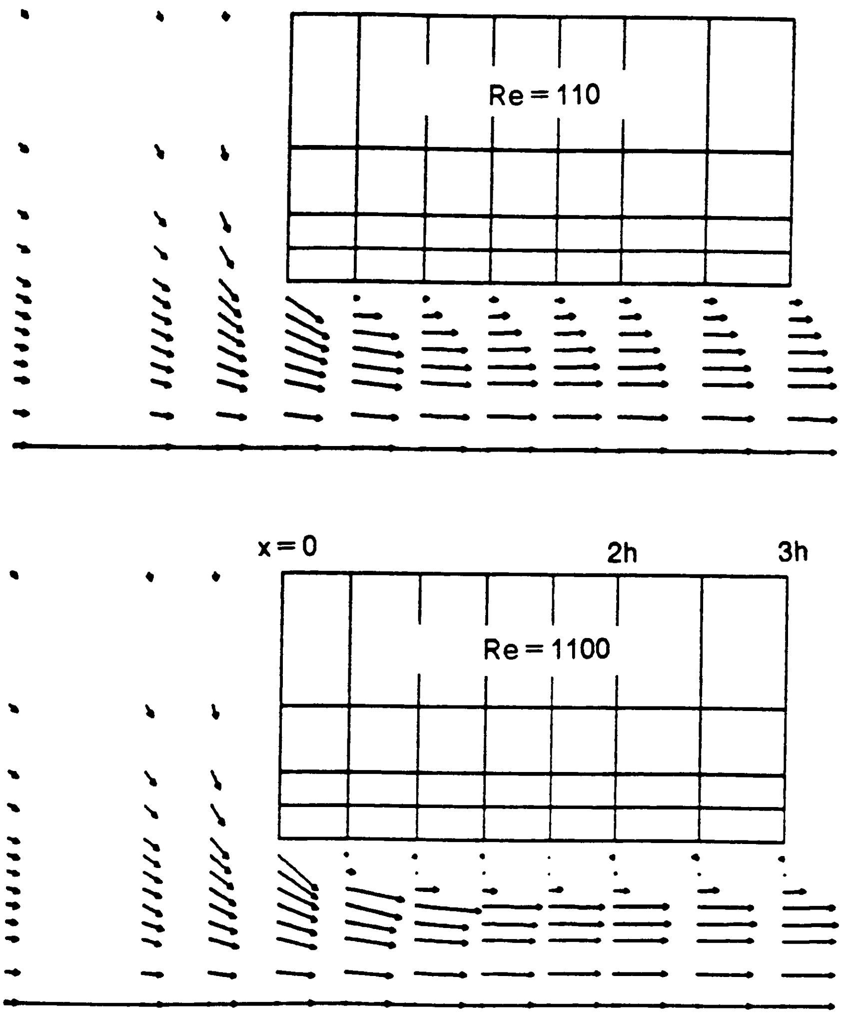

Figure 5. Moore's calculated laminar tip gap flow

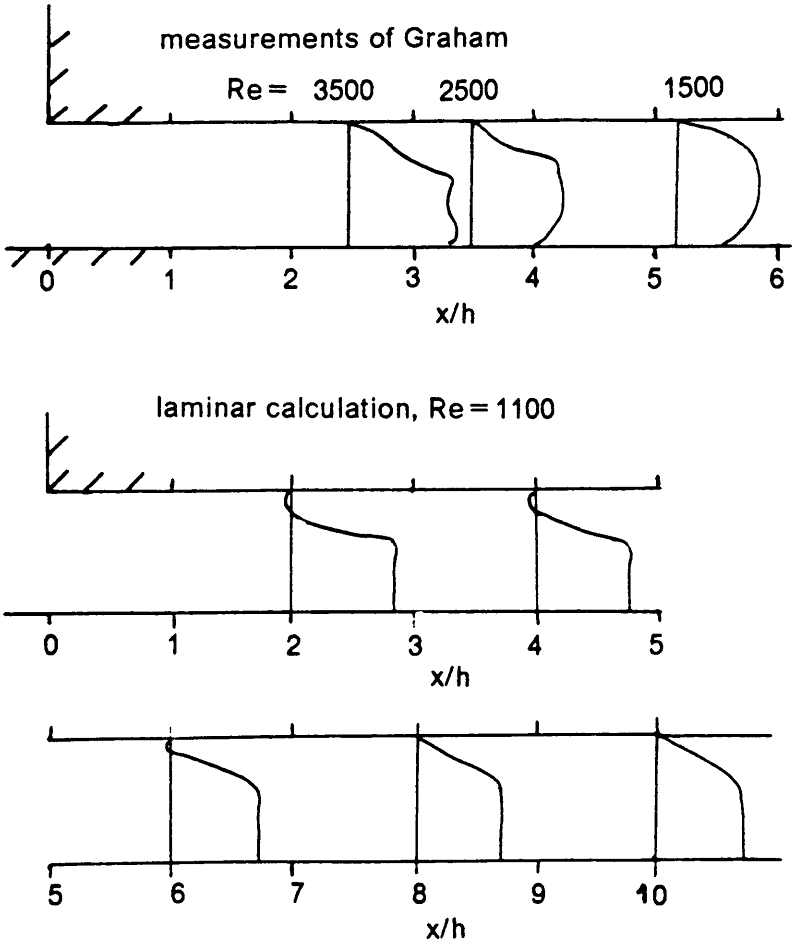

Figure 6. **Comparison of Graham's measured and Moore's calculated velocity profiles**

image. In doing so, Henry achieved an inviscid boundary at the shroud wall (centerline). Measurements of the water surface heights along the centerline (shroud wall) were taken for various back pressure ratios.

Using the hydraulic analogy, water height ratios were converted to corresponding pressure ratios and Mach numbers for a compressible gas flow with $k=1.4$. The hydraulic analogy will be explained in the section following. Figure 7 shows a plot of these quantities versus position from channel inlet in terms of channel half widths or, equivalently, tip gap heights. A top view of the wave patterns observed for four of these cases is sketched in Fig. 8.

The curves in Fig. 7 show that as the back pressure is reduced, the flow in the tip gap becomes supersonic at a back pressure ratio $\frac{P_b}{P_0}$ of about 0.70. Further lowering the back pressure causes higher and higher maximum Mach numbers, with flow becoming subsonic again within two tip gap heights. This is associated with a Mach reflection at the centerline as sketched in part b of Fig. 8. The return to subsonic flow after the minimum pressure is no longer observed after $\frac{P_b}{P_0}$ of about 0.50. For back pressures ratios below 0.50, oblique shocks are observed reflecting at the centerline with all flow downstream remaining supersonic.

Hydraulic Analogy

In order to translate his water table results into useful compressible flow ideas, Henry makes use of the hydraulic analogy. The hydraulic analogy will be presented here in

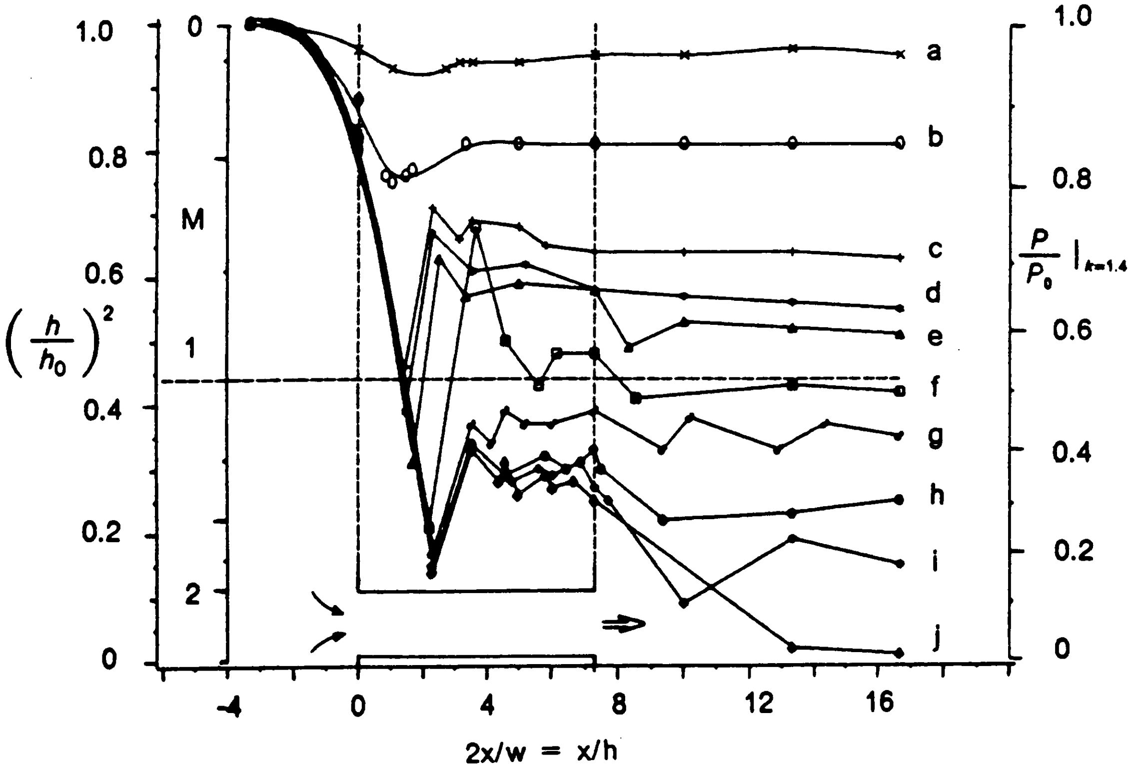

Figure 7. Henry's hydraulic analogy pressure ratios and isentropic Mach numbers

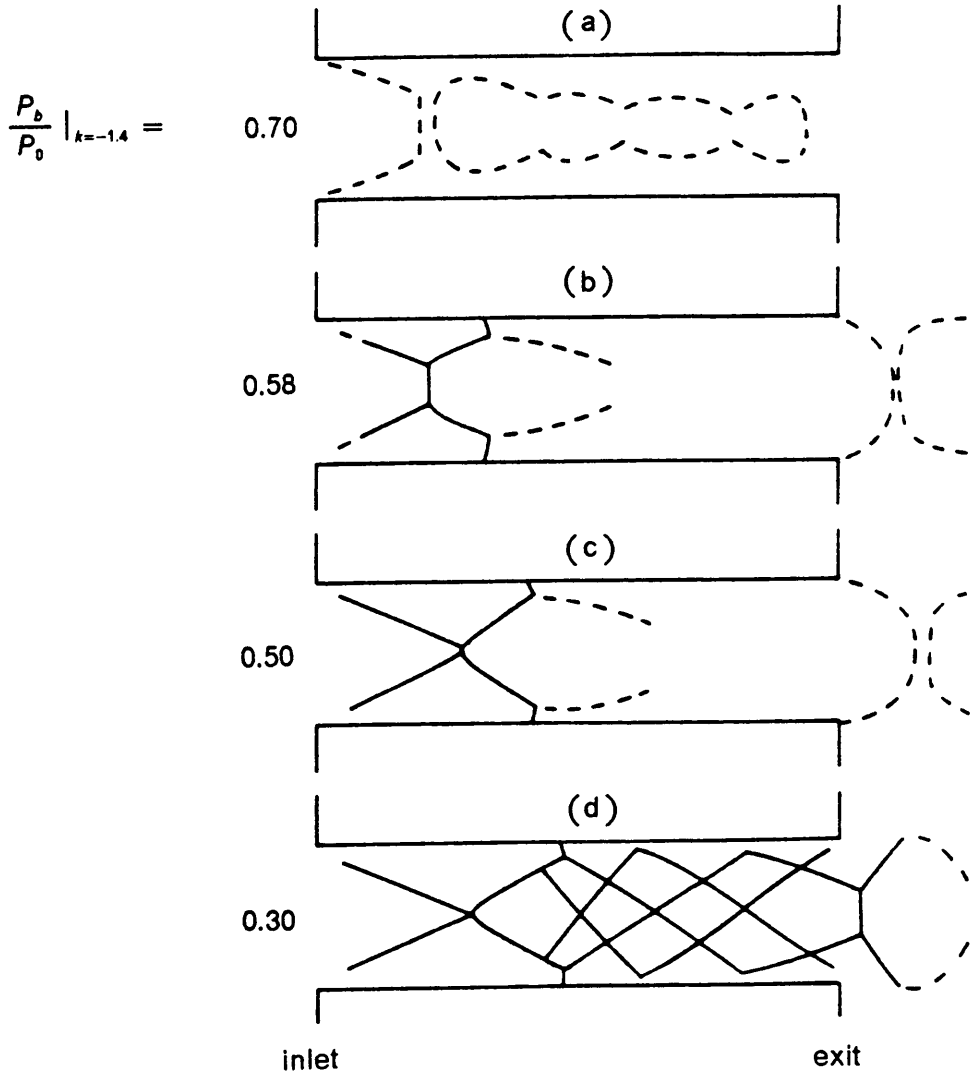

Figure 8. Sketches of channel surface waves (Henry)

two parts. First, the classical analogy, as used by Henry, and then a modified analogy which was found to be more relevant to the present work.

Classical Analogy

Page [7] gives the equation for the velocity of a wave moving on the surface of a fluid to be

$$V = \sqrt{\left(\frac{g\lambda}{2\pi} + \frac{2\pi T}{\rho\lambda} \right) \tanh\left(\frac{2\pi h}{\lambda} \right)} . \tag{1}$$

As seen from this equation, two factors affect the wave velocity, gravity ($\frac{g\lambda}{2\pi}$) and surface tension ($\frac{2\pi T}{\rho\lambda}$). Neglecting surface tension for the moment, the equation becomes

$$V = \sqrt{\frac{g\lambda}{2\pi} \tanh\left(\frac{2\pi h}{\lambda} \right)} .$$

The limiting case of shallow water ($h << \lambda$) is of interest here. In this case, $\frac{2\pi h}{\lambda} \rightarrow 0$ so $\tanh\left(\frac{2\pi h}{\lambda} \right) \rightarrow \frac{2\pi h}{\lambda}$. Thus, the wave velocity becomes a function of water depth only:

$$V = \sqrt{gh}$$

which is similar in form to the equation for the speed of sound in an ideal gas:

$$c = \sqrt{kRT} .$$

To find the analogous properties between the two types of flows, consider a reversible decrease in depth for a water flow and a reversible gas expansion as shown in Fig. 9.

Applying the conservation of energy along a streamline in the water flow,

$$\frac{P_0}{\rho} + gz_0 = \frac{P}{\rho} + gz + \frac{V^2}{2}$$

or

$$V^2 = 2\frac{(P_0 - P)}{\rho} + 2g(z_0 - z).$$

Assuming that the static pressure is due only to the hydraulic pressure, $P_0 = \rho g(h_0 - z_0)$ and $P = \rho g(h - z)$ then the expression for velocity becomes

$$V^2 = 2g(h_0 - h)$$

The maximum velocity this flow can achieve is $\sqrt{2gh_0}$ or

$$V_{\max}^2 = 2gh_0.$$

Dividing V by $V_{\max}$ will yield

$$\left(\frac{V}{V_{\max}}\right)^2 = \frac{h_0 - h}{h_0}. \qquad (2)$$

Next, applying the first law to the reversible gas expansion for an ideal gas,

$$H_0 = \frac{V^2}{2} + H$$

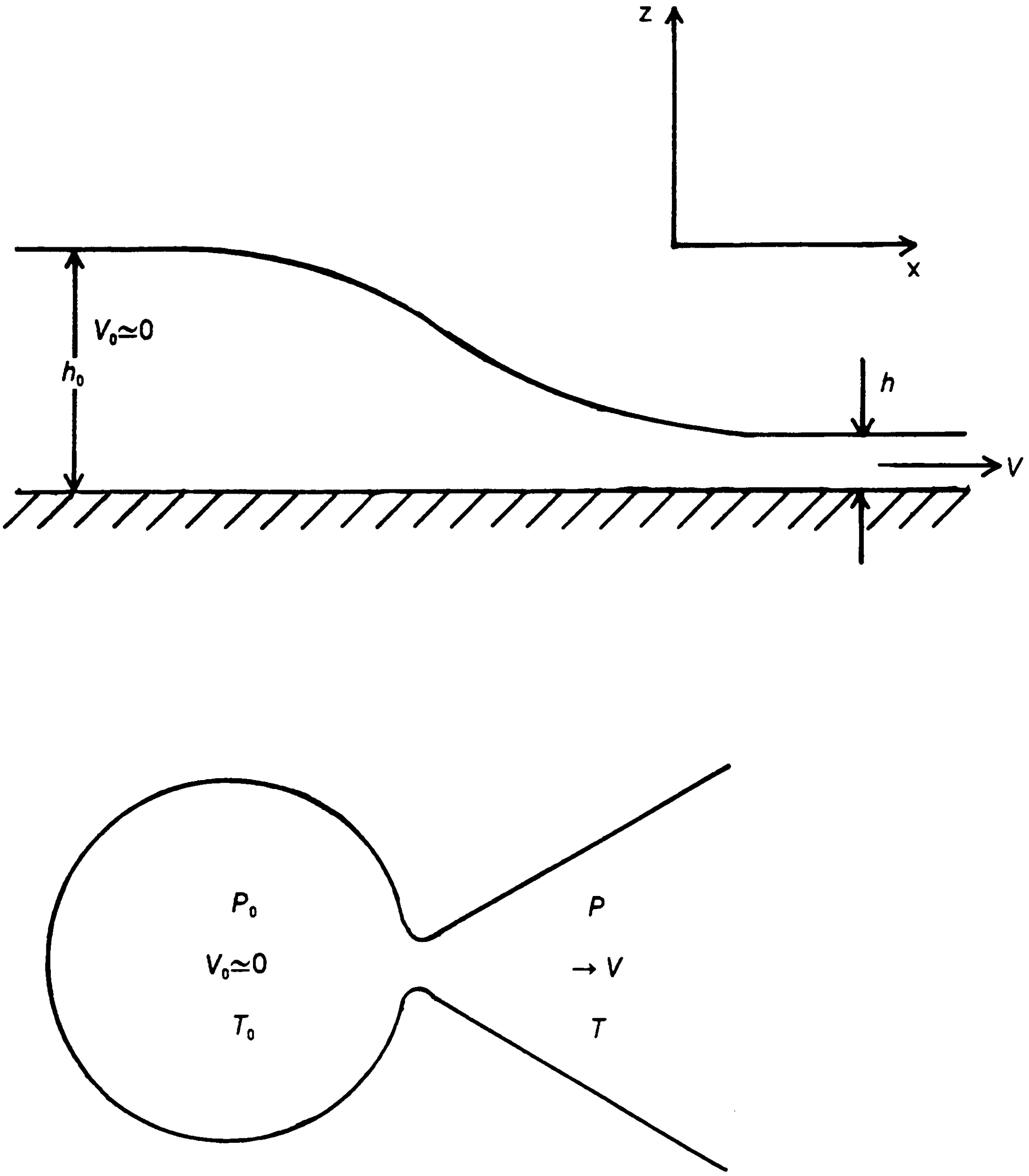

Figure 9. Analogous reversible processes for water and gas flows

$$V^2 = 2(H_0 - H)$$

$$V^2 = 2C_p(T_0 - T).$$

The maximum velocity possible here is $V_{max} = 2C_pT_0$ so that

$$\left(\frac{V}{V_{max}}\right)^2 = \frac{T_0 - T}{T_0} \qquad (3)$$

If equations 2 and 3 are made equal,

$$\frac{h_0 - h}{h_0} = \frac{T_0 - T}{T_0}$$

then

$$\frac{h}{h_0} = \frac{T}{T_0} \quad .$$

Continuity is applied to both flows yielding

$$\frac{\partial(hu)}{\partial x} + \frac{\partial(hv)}{\partial y} = 0$$

for water and

$$\frac{\partial(\rho u)}{\partial x} + \frac{\partial(\rho v)}{\partial y} = 0$$

for gas. These equations will be the same if ρ and h are analogous. Therefore it can be stated that

$$\frac{h}{h_0} = \frac{\rho}{\rho_0}.$$

The isentropic perfect gas relations give

$$\frac{T}{T_0} = \left(\frac{\rho}{\rho_0}\right)^{k-1}$$

If both T and ρ are analogous to h, then k-1 = 1 or k = 2. Therefore, it follows that the hydraulic analogy will give results for a gas with a ratio of specific heats, k = 2.

Given that k = 2, $\frac{h}{h_0} = \frac{\rho}{\rho_0}$, and knowing that for isentropic flow

$$\frac{P}{P_0} = \left(\frac{\rho}{\rho_0}\right)^{k},$$

then

$$\frac{P}{P_0} = \left(\frac{h}{h_0}\right)^{2}$$

or

$$\frac{h}{h_0} = \sqrt{\frac{P}{P_0}}.$$

A number similar to the Mach number can be developed for the water flow. Taking the ratio of water velocity to surface wave velocity yields

$$\frac{V}{\sqrt{gh}} = \sqrt{\frac{2g(h_0 - h)}{gh}}$$

$$= \sqrt{2\left(\frac{h_0}{h} - 1\right)}$$

This is known in hydraulics as the Froude number, F. A height ratio of $\frac{h}{h_0} = \frac{2}{3}$ will give F = 1, or critical flow. The analogous quantities are summarized in Table 1.

For the above development, the surface tension term in equation (1) was neglected. In doing so, the effect of capillary waves was ignored. Capillary waves arise when the surface of the water vibrates as a membrane. Johnson [8] reports that reducing the surface tension as much as possible will help lessen the effect of these waves.

Figure 10 is a plot of wave velocity as a function of wavelength λ and water depth h as given by equation (1). This plot is for tap water with surface tension of 70 dynes/cm. It shows the effect of the surface tension term of equation 1. For small wavelengths, the velocity of the surface wave tends toward infinity. If the surface tension term is neglected, the velocities will approach zero for smaller and smaller wavelengths. As λ increases, the velocity approaches $\sqrt{gh}$. Since this is the velocity used in the analogy, it is important to run experiments in the range where velocity is not a function of wavelength--at larger wavelengths and/or more shallow depths. From Fig. 10, depths of between 0.5 cm and 1 cm are best. This observation agrees with Johnson's experimental experience.

Laitone [9] suggests that reducing surface tension may adversely affect the analogy. However, reducing the surface tension will reduce the velocity of the capillary waves. Figure 11 is a plot similar to Fig. 10 except the surface tension has been reduced to

Table 1. Analogous quantities of the hydraulic analogy

liquid flow	gas flow
surface wave velocity, $V = \sqrt{gh}$	speed of sound, $c = \sqrt{kRT}$
water depth ratio, $\frac{h}{h_0}$	temperature ratio, $\frac{T}{T_0}$
water depth ratio, $\frac{h}{h_0}$	density ratio, $\frac{\rho}{\rho_0}$
water depth ratio squared, $\left(\frac{h}{h_0}\right)^2$	pressure ratio, $\frac{P}{P_0}$
Froude number, $\sqrt{2\left(\frac{h_0}{h} - 1\right)}$	Mach number, $\frac{V}{c}$

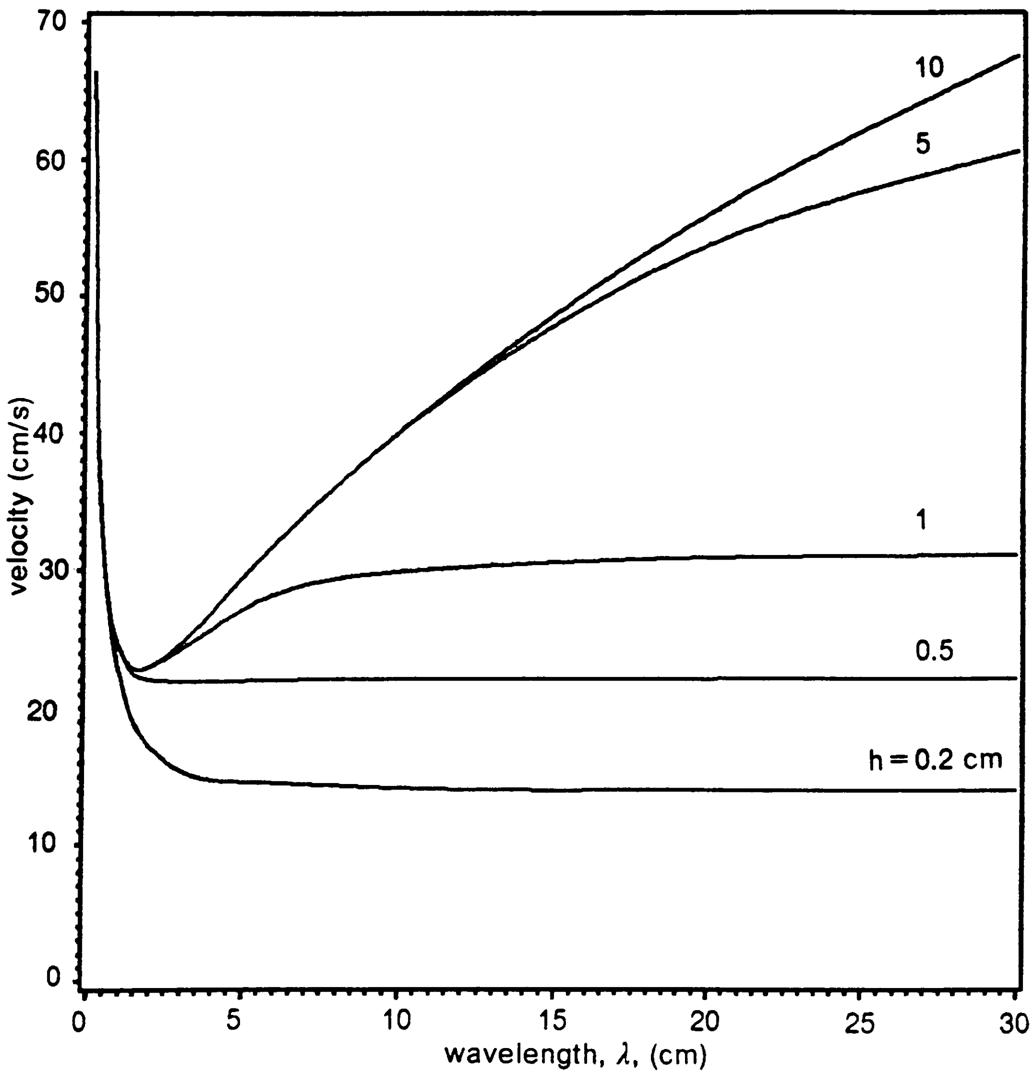

Figure 10. Wave velocity as a function of wavelength and water depth: T = 70 dynes/cm

30 dynes/cm. It is clear that reducing the surface tension has adversely affected the analogy since the velocity does not approach $\sqrt{gh}$ as quickly. Figure 11 also shows that waves of shorter wavelength (i.e. capillary waves) have a smaller velocity. This will slow down the capillary waves so they approach the gravity wave, the wave of interest in the analogy. Thus a reduction in surface tension will work in lessening the effect from the capillary waves. This was the observed result in the present tests.

Laitone also suggests that the effect of capillary waves may be all but neglected by using a larger model. Since the oblique hydraulic jumps described in the next section are a function of flow physics alone, it was not clear to the author that a larger model would ensure larger wavelengths. Thus it was decided to examine the effect of relative model size on the flow.

Modified Hydraulic Analogy

A fundamental requirement of the classical hydraulic analogy is that the flow be isentropic. However, this requirement is violated when shocks are present. As a result, the classical analogy leads to large errors.

Ippen [10] proposed a modification to the classical analogy which can provide a much better quantitative agreement. He considered two flows, one water and one gas. Both flows are deflected by a wall which turns the flow, as shown in if Fig. 12. Such a deflection can cause an oblique shock in the gas flow and an oblique hydraulic jump in the water flow. Given the inlet Mach number (gas) or Froude number (water) and deflection angle (δ) , the resulting shock angle (σ) or jump angle (β) , can be determined by the following relations:

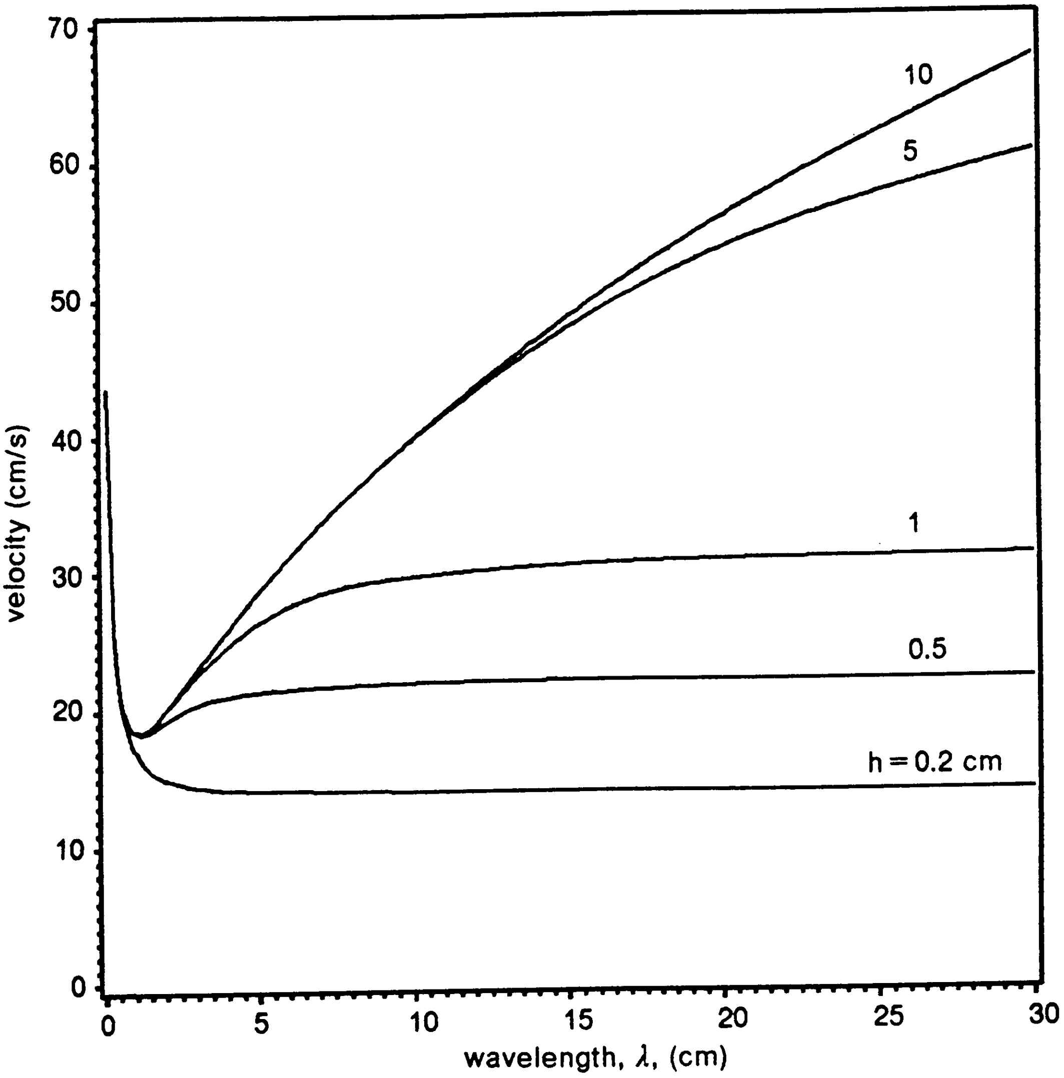

Figure 11. Wave velocity as a function of wavelength and water depth: T = 30 dynes/cm

$$\tan\delta = \frac{\tan\beta(\sqrt{1+8F^2\sin^2\beta}-3)}{2\tan^2\beta+\sqrt{1+8F^2\sin^2\beta}-1}$$

and

$$\tan\delta = \frac{(M^2\sin^2\sigma-1)\cot\sigma}{\frac{k+1}{2}M^2-M^2\sin^2\sigma+1}$$

The development of these equations appears in Appendix A. Then σ can be used, with k = 1.4, to find the appropriate ratios of $\frac{P_2}{P_1}$, $\frac{\rho_2}{\rho_1}$, and $\frac{T_2}{T_1}$ across the shock and β can be used to find the corresponding $\frac{h_2}{h_1}$ across the jump.

Figure 13 shows a plot of these ratios versus Mach/Froude number resulting from a 9° deflection. It is evident that the density ratio is the only aerodynamic ratio which agrees reasonably well with $\frac{h_2}{h_1}$. Ippen found that by using the height ratio as the density ratio in the aerodynamic relations, the other aerodynamic ratios-- $\frac{P_2}{P_1}$ and $\frac{T_2}{T_1}$ --could be obtained within 5 percent.

Compressible Orifice Flows

Although little was found in the literature about compressible tip gap flows, much research had been done with compressible orifice flows. Benson and Pool [11] give a fairly detailed description of early research in this area.

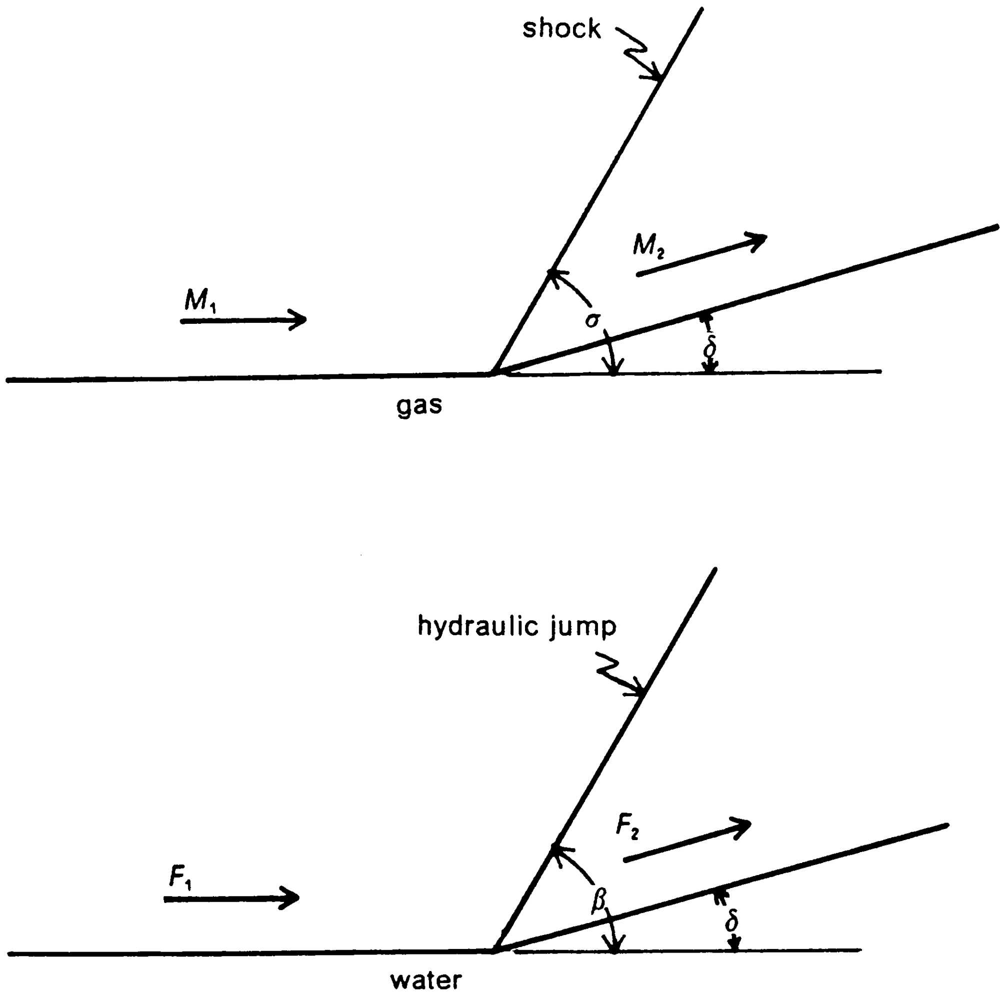

Figure 12. Supercritical water flow and supersonic gas flow over a wedge

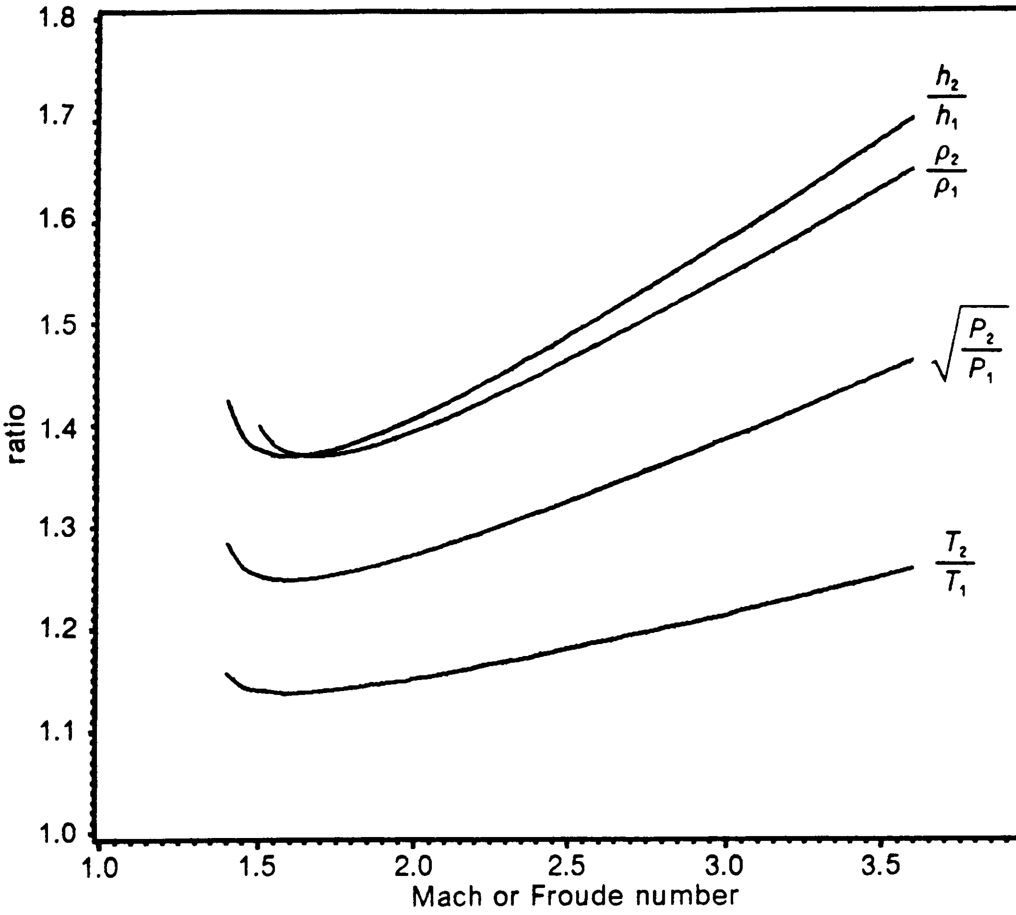

Figure 13. Comparison of aerodynamic and hydrodynamic shock relations: $\delta = 9°$

Benson and Pool numerically solved the equations of steady, isentropic, compressible flow through a two-dimensional slit. They then compared the results with Schlieren photographs and interferograms.

Figure 14 shows flow through a half orifice in both the physical and hodograph planes. A qualitative discussion of Fig. 14 is presented here. The flow accelerates along the orifice wall to point B (stage 1). If the upstream pressure is high enough, the flow will undergo a Prandtl-Meyer expansion at B to the freestream velocity. Line EC in the physical plane represents the "last characteristic", as it is the last one to intersect the sonic line. Any wave downstream of EC will not affect the upstream flow. The velocity then increases along line CF (stage 2) to point F on the free streamline. In the hodograph plane, a discontinuity occurs in the streamline, deflecting it into region CFG (stage 3). The velocity now increases to point G (stage 4), the point of maximum velocity in the flow. Following line GH, the velocity decreases below the freestream value (stage 5). The end of stage 5 is the hodograph characteristic HI which coincides with characteristic EC from stage 2. The streamline pattern in stage 5 is different from that in stage 2 and thus the pattern of constant velocity lines will be different. Discontinuity in the slope of the velocity lines may result in a shock. Ideally, the pattern from CF to IJ would be repeated indefinitely downstream of IJ.

The flow fields for pressure ratios of 0.1234 and 0.075 determined graphically by Benson and Pool are shown in Fig. 15. Of particular interest here are the shapes of the free streamlines and the sonic lines. The free streamlines in each case come off the orifice edge sloping into the orifice in a downstream direction. The streamlines then curve upward, their slopes increasing in the direction of flow as noted in the figure as segment EF. Eventually, the slopes of the free streamlines flatten out and

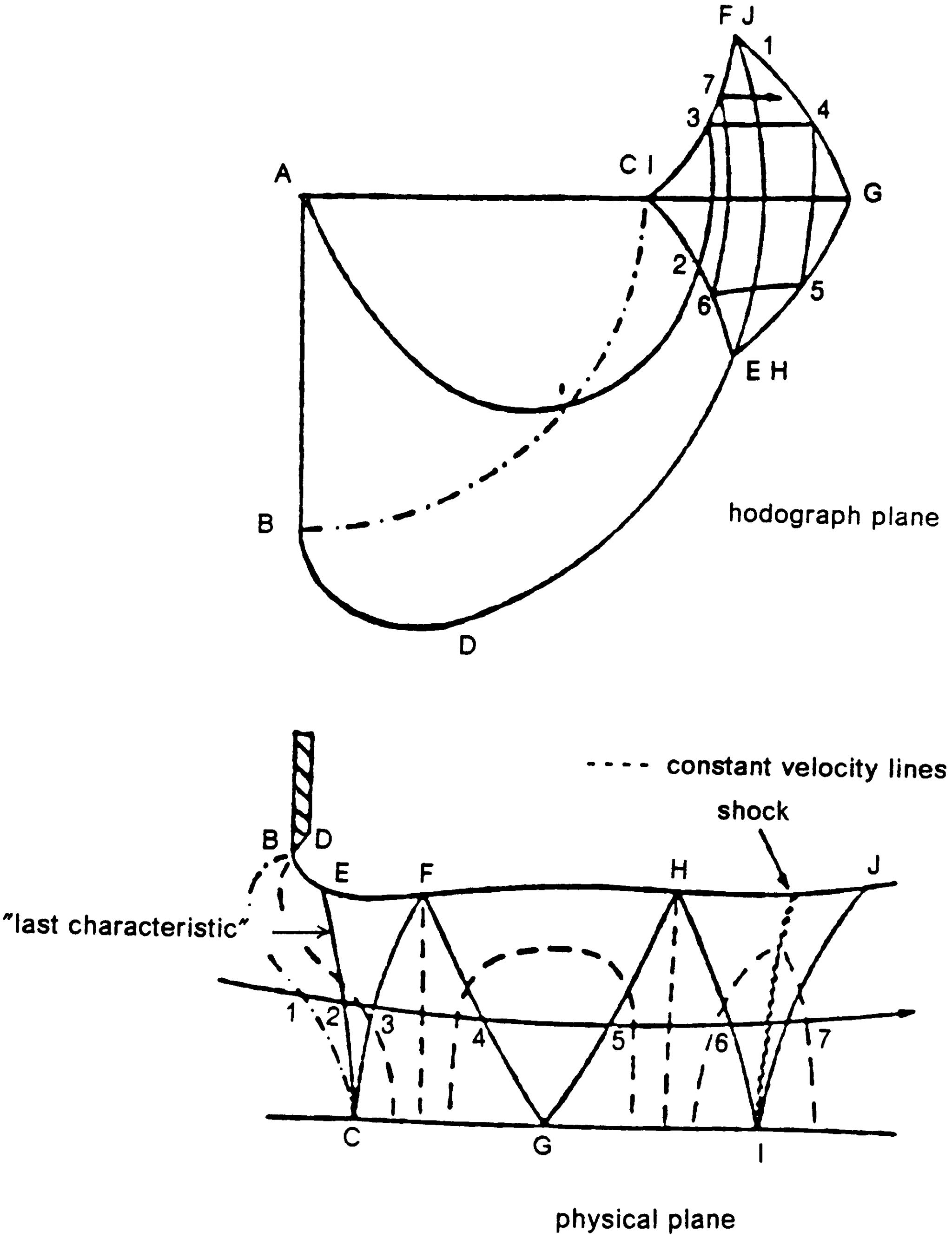

Figure 14. The hodograph and physical representation of flow through a slit

begin to decrease. This gives the jet its shape. Figure 15 shows that as the pressure ratio is reduced, the slope of the free streamline increases more rapidly producing a more severe turn in the free streamline. The sonic lines come off the orifice edge in a slightly upstream direction before curving back and moving inward. The sonic lines then intersect the centerline of the orifice at right angles.

Benson and Pool also discuss three types of shocks which can be present in supercritical flow in the jet. These can be seen in Figs. 16, 17, and 18. Figure 16 shows the first type of shock associated with the discontinuities of the constant velocity lines. This shock occurs at pressure ratios near the critical value. As the back pressure is lowered, the shock moves downstream as can be seen in Fig. 17. Figure 18 shows the case for very low back pressures. The weak incident shocks are seen undergoing a regular reflection to produce a strong, curved shock. All these shocks occur far downstream of the sonic line and section EF of the free streamline.

At about the same time Benson and Pool were doing their work, Norwood [12] was conducting similar work. He calculated the flow in transonic gas jets, modeling flow through an infinite slit. In addition, Norwood performed experiments on jet reattachment in a flapper valve.

Figures 19 and 20 show the results of Norwood's calculations. Figure 19 plots the position of the sonic line for various back pressures. The sonic line is seen starting at the orifice edge, heading slightly upstream and then curving back and heading in the downstream direction for all cases. The lower the back pressure, the farther upstream the sonic line moves before heading in the downstream direction. As the sonic lines curve downstream, they intersect the orifice centerline perpendicularly. For higher back pressures, the intersection of the sonic line with the centerline

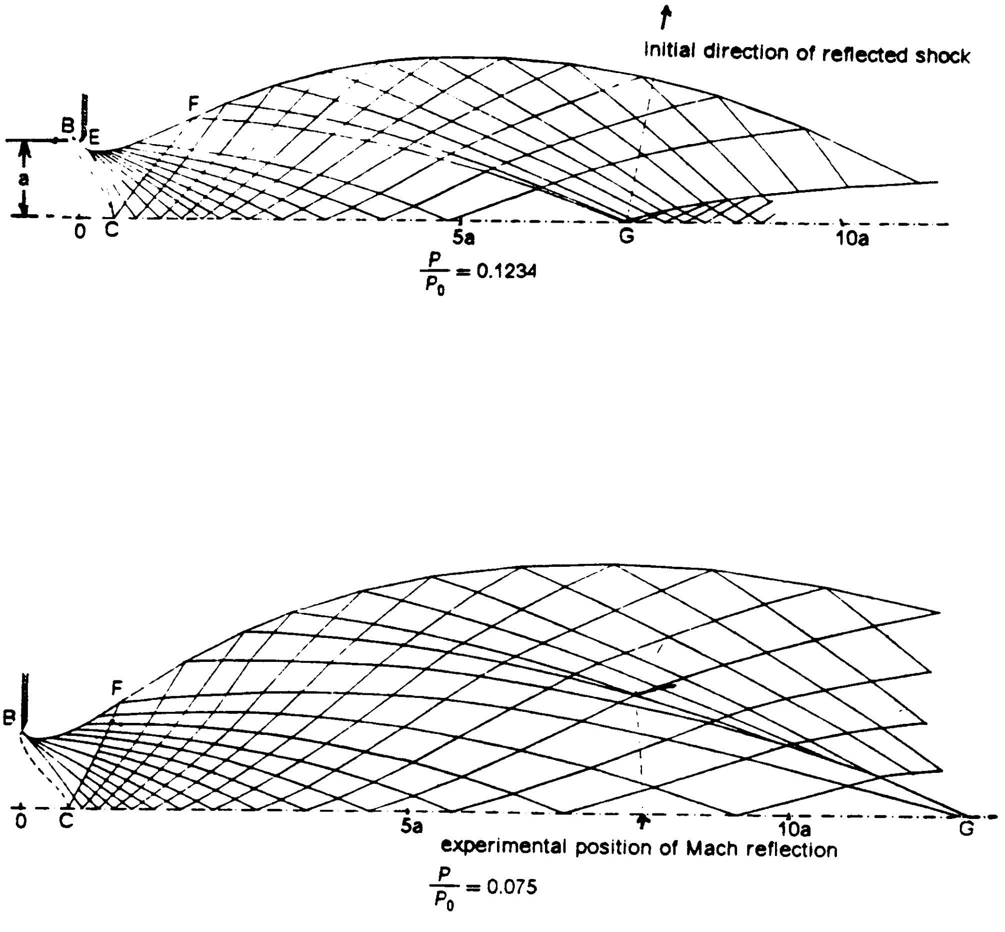

Figure 15. Benson and Pool's graphically determined flow fields

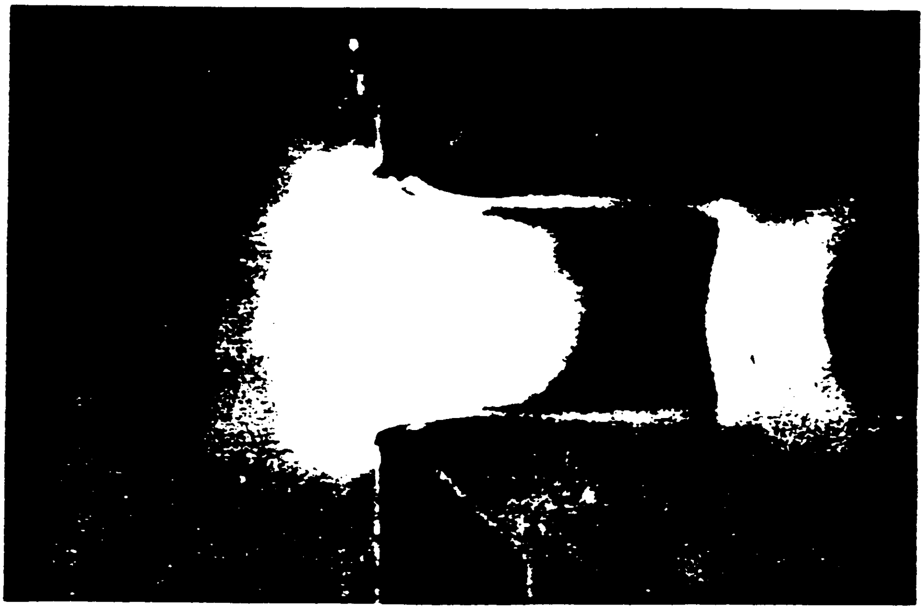

Schlieren photograph, $\frac{P}{P_0} = 0.4250$

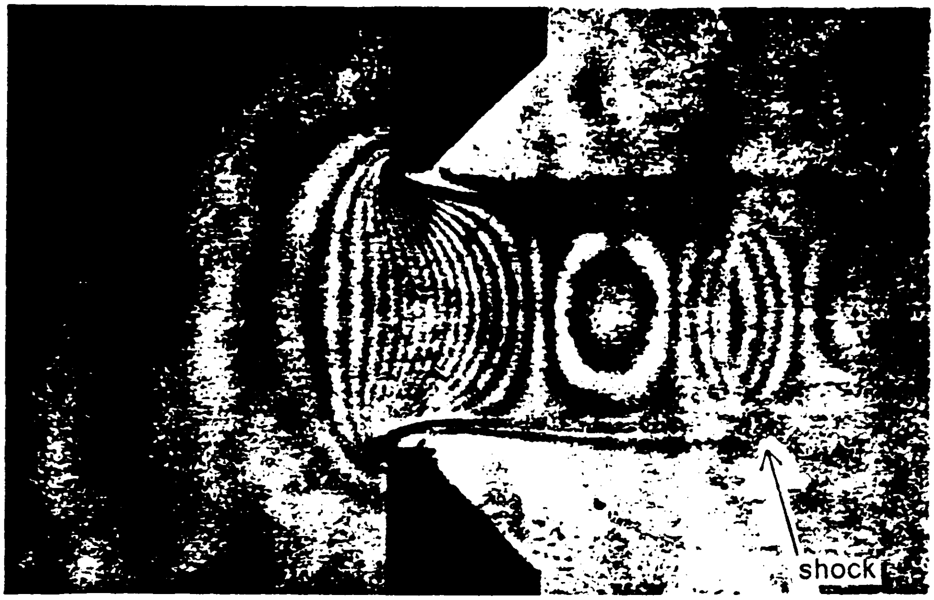

Interferogram, $\frac{P}{P_0} = 0.4250$

Figure 16. Schlieren and Interferogram of flow through a slit, Benson and Pool

Schlieren photograph, $\frac{P}{P_0} = 0.227$

Schlieren photograph, $\frac{P}{P_0} = 0.123$

Figure 17. Schlieren photographs of flow through a slit, Benson and Pool

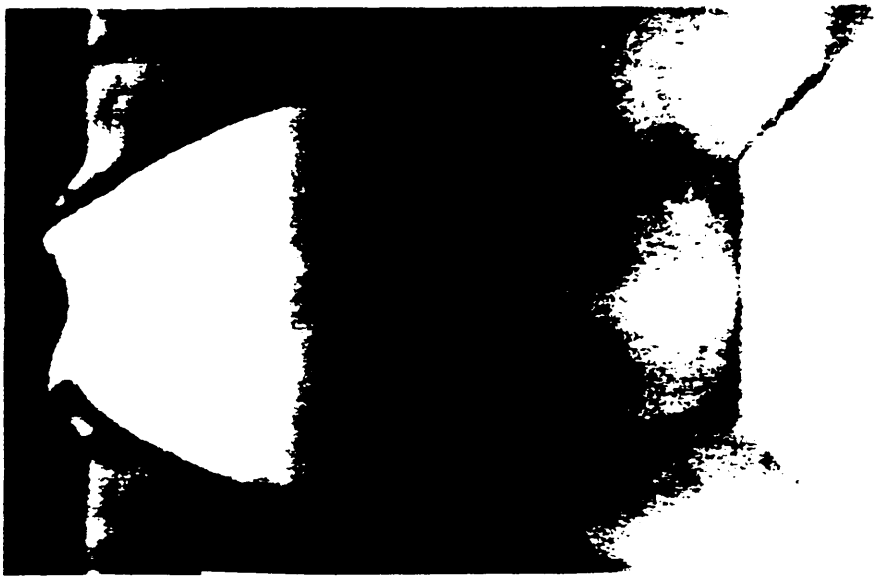

Schlieren photograph, $\frac{P}{P_0} = 0.100$

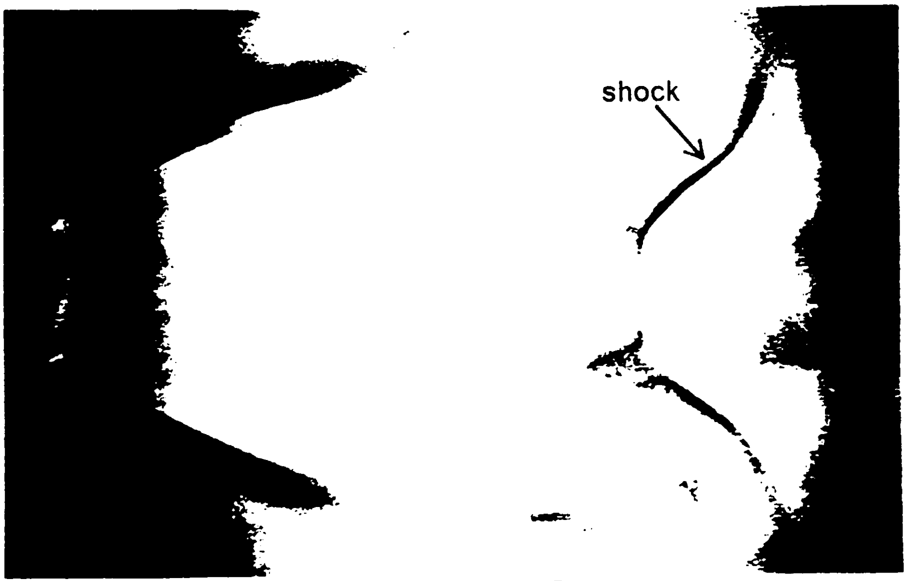

Schlieren photograph, $\frac{P}{P_0} = 0.075$

Figure 18. Schlieren photographs of flow through a slit, Benson and Pool

occurs farther downstream. The line of $\frac{P}{P_0} = 0.039$ is the limiting case, corresponding to choked flow.

In Fig. 20, the position of the free streamline is shown for the same pressure ratios used in Fig. 19. The shapes of the free streamlines are similar to those determined graphically by Benson and Pool. The free streamline comes off the orifice edge sloping downward at an angle and then curves upward. As the pressure ratio is reduced, the angle of slope coming off the orifice edge is smaller and the free streamline turn is more abrupt. In all cases, the streamline is turned through ninety degrees from coming off the orifice edge to the point of its maximum slope. In this case the position of the free streamline will continue to change below pressure ratios of 0.039.

Norwood's experimental work was done on a two-dimensional model of a flapper valve. Figure 21 contains shadowgraphs of flow in the model. In the top picture, the flow is seen along the horizontal wall. This corresponds to a case of high back pressure. The flow expands around the corner with the jet mixing out downstream. As the back pressure drops, the free streamline will curve upward as the calculations in Fig. 20 show. At a low enough pressure ratio, the free streamline will contact the upper wall, causing a turn in the flow. This will give rise to a shock, as can be seen in the bottom picture of Fig. 21. Figure 21 also shows a shock on the horizontal wall of the model. As the flow moves along the horizontal wall up to the point of the shock, it is alternately accelerated and decelerated. Eventually the rising pressure gradient will cause the flow to be deflected upward, resulting in the lower shock. At this point, the flow is entirely along the upper wall.

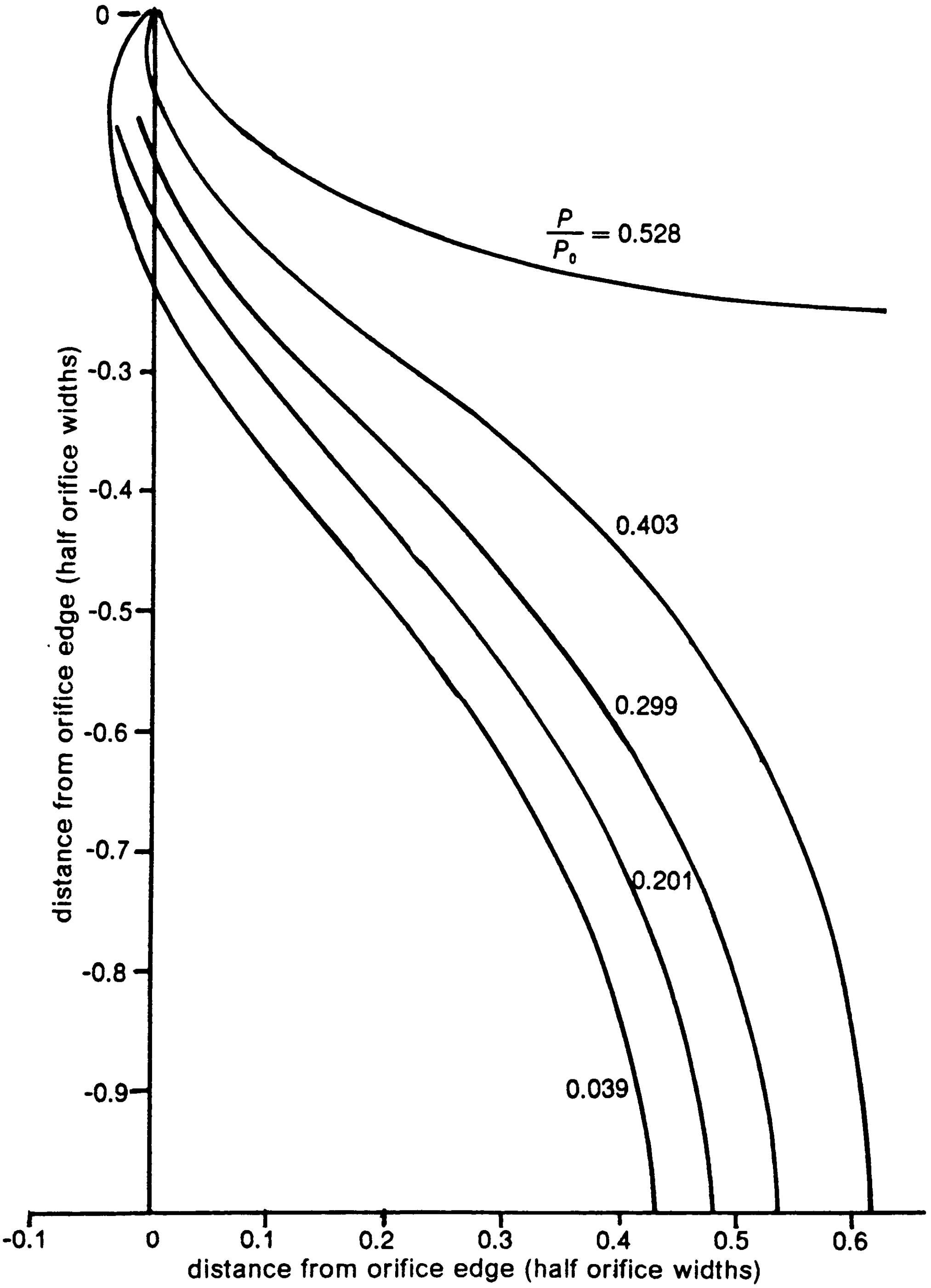

Figure 19. Norwood's calculated sonic lines for flow through an infinite slit

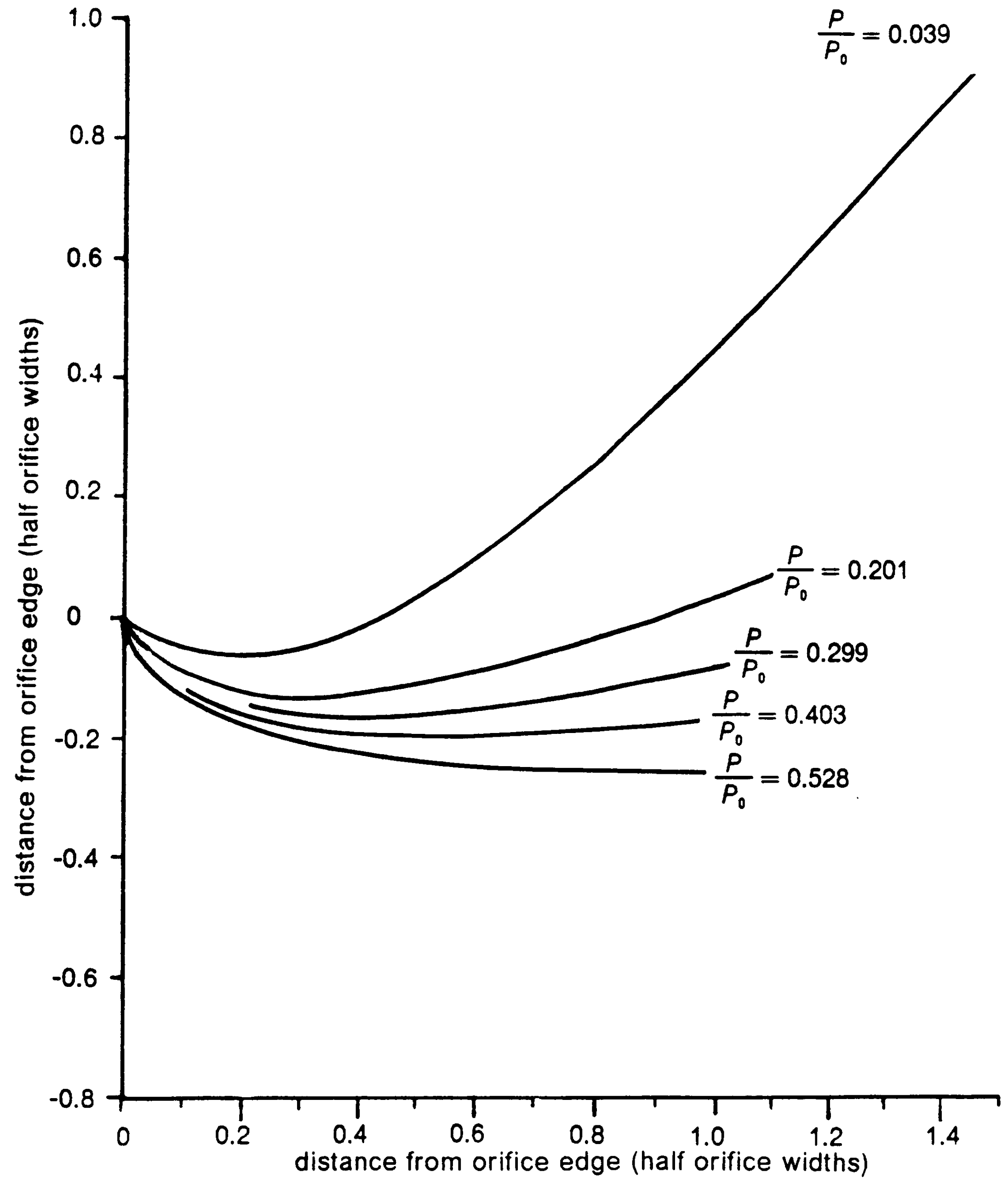

Figure 20. Norwood's calculated free streamline shapes

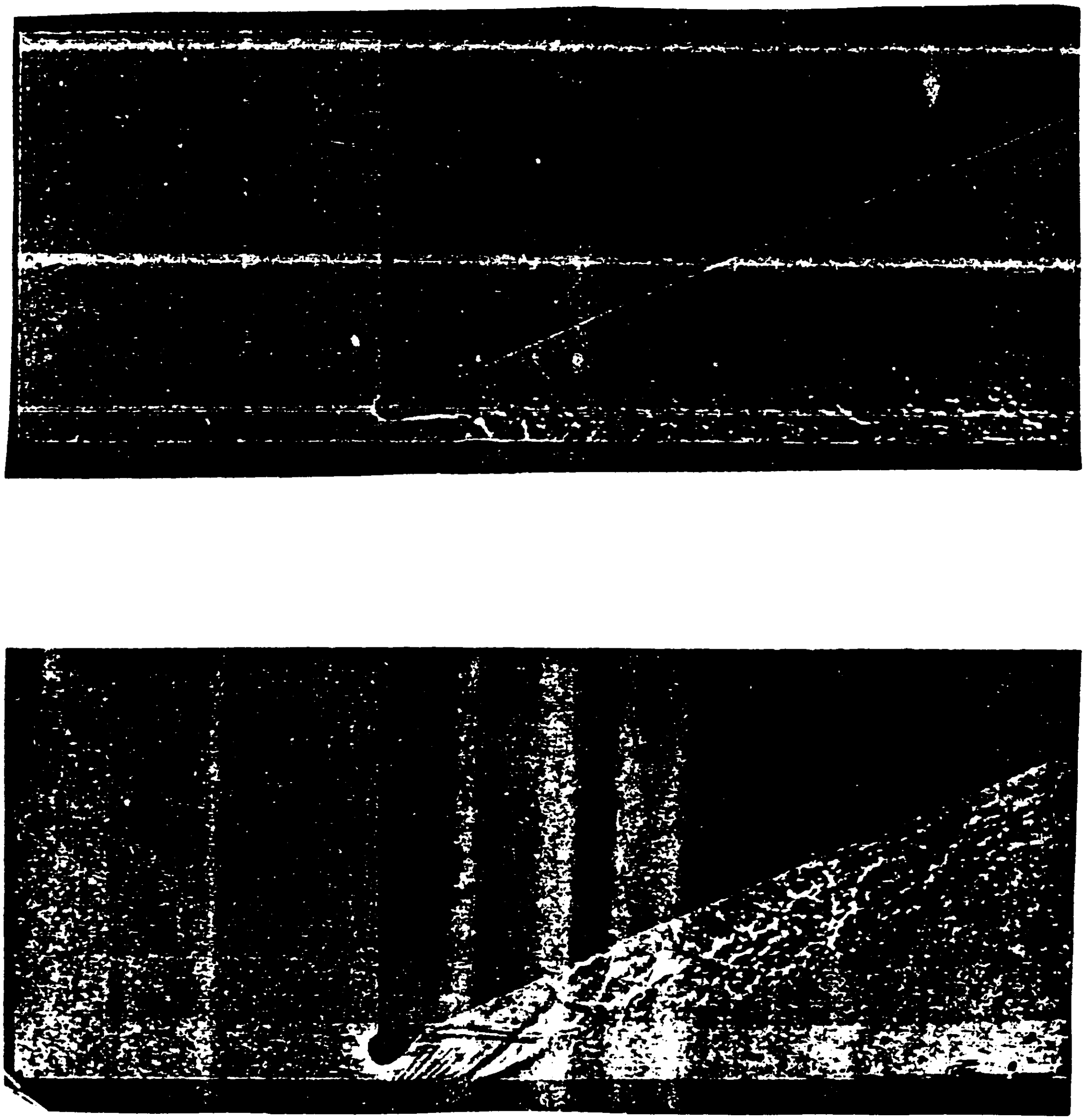

Figure 21. Shadowgraphs of Norwood's flapper valve flow

Norwood's observations seem to provide an explanation for Henry's results. At lower back pressures, the shape of the free streamline is such that the flow is turned by the channel walls. The result is an oblique shock near the channel entrance.

This investigation will study the mechanism of the shock observed by Henry using the insights provided by Norwood. The study will be performed on the same water table used by Henry, with some modification. In addition to the effects of flow conditions on the shock formation, the role of size and scaling of the hydraulic model on the formation of a hydraulic jump will be examined.

Chapter III

Experimental Apparatus and Procedure

Water Table

The water table apparatus used in this study is sketched in Fig. 22. The table itself consists of two large tanks each about 0.22 m^3 in volume on either end of a glass table of dimensions 0.91 x 0.61 m. Each of the four table legs can be independently adjusted for leveling by means of an adjustment bolt. In addition, the upstream end of the table can be raised and lowered by a screw/wedge system.

Flow across the table is provided by the pump as shown. The rotameter was installed so the flow could be monitored and reproduced. A filter was added to the original system to keep the water clean. To regulate the flow, the throttle valve downstream of the pump is used. A sluice gate at the downstream end of the table is used to maintain the desired water height on the table.

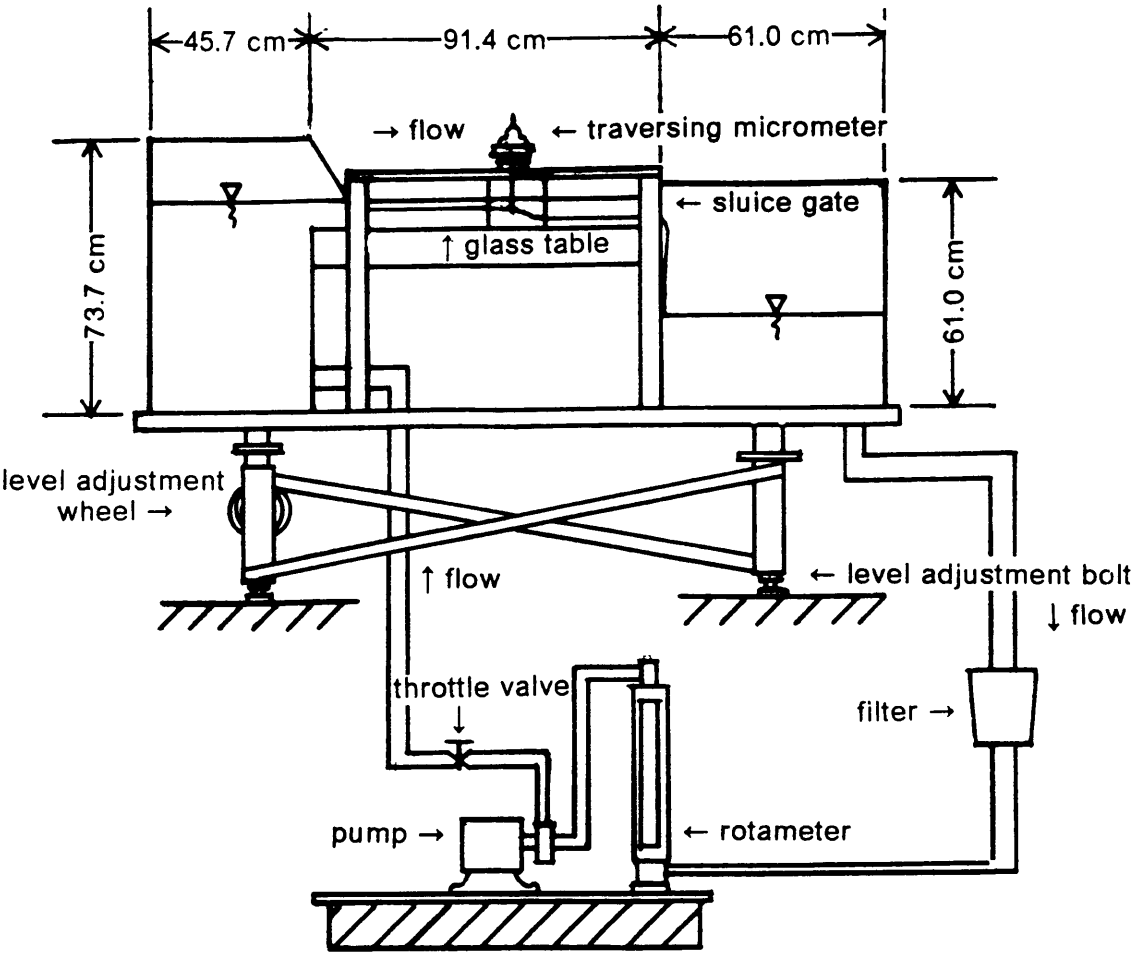

Figure 22. Sketch of water table apparatus

Measurement of the water heights was accomplished by a traversing micrometer with a least count of 0.001 in (0.0254 mm). The micrometer is mounted on rails which allow it to traverse in both the longitudinal and latitudinal directions. Distances in either direction were measured with 0.1 in (2.54 mm) least count scales, each fitted with a vernier scale allowing measurement to the nearest 0.01 in (0.254 mm). The pointer of the micrometer is a long brass rod. This rod was not exactly straight and a wobble was present when the rod was turned. As a result, the location of the probe is known only to within 0.03 in (0.76 mm).

To ensure that the vertical accelerations are negligible, the water table was leveled using the four adjustment bolts. First, the table was filled with water and allowed to settle. The water height was measured at the four corners of the table as determined by the limit of range of travel of the micrometer, 63.8 cm x 44.3 cm. Then adjustments were made to the bolt or bolts which required changes. The water heights were again checked at the corners. This was repeated until the water heights at each of the four corners were as equal as possible. The table was level to within 0.25 mm across the entire table surface. Since the various test sections used were no larger than 19.8 x 7.6 cm, the table within the test section was be level to well within about 0.08 mm.

As mentioned previously, it is desirable to reduce the surface tension of the water as much as possible. Johnson reports using photographic wetting agents to accomplish this. The Learning Resources Center at Virginia Tech provided the author with Kodak Photoflo 600 which was used to reduce the surface tension in this case. Figure 23 shows the result of adding the Photoflo to regular tap water. The method used to determine the surface tension is detailed in Appendix B. When running the water table tests, surface tension was kept at about 30 dynes/cm.

Test Sections

The test sections used for this investigation were all assembled using two aluminum blocks machined in the Mechanical Engineering machine shop at Virginia Tech. The drawing for one of these blocks is shown in Fig. 24. The corner at the leading edge (entrance to the channel) was machined as sharp as possible to ensure an entrance modelling a sharp edge orifice. Also, the front face (channel sidewall) and upstream side of the blocks were machined smooth to avoid interference with the flow. The dimensions marked a and c were determined by the availability of material, while the dimension marked b was made to give a desired channel width.

The width of the chosen channel was determined based on the desired wave structure in the channel. Ippen states that similarity of flow geometry is not possible if the flow contains shocks (i.e. waves) of different intensities. It was therefore decided to make the channel such that the waves formed at the corners of the channel entrance intersected within the channel, but their reflections from the channel center did not intersect the channel wall. A representative sketch of the test section is shown if Fig. 25. The desired flow regime is also sketched within the test section of Fig. 25. The location of the origin and the axes chosen to measure channel coordinates are also shown in the figure.

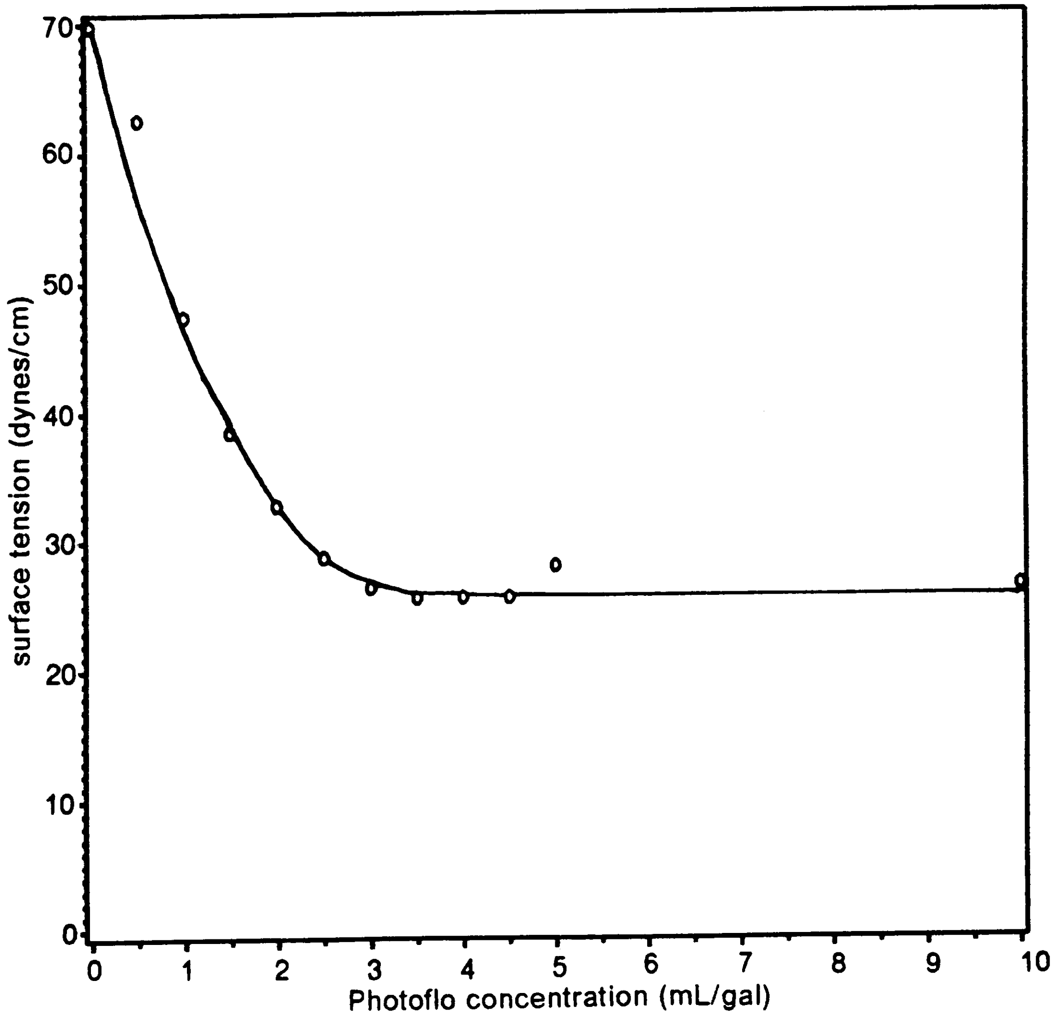

Figure 23. **Surface tension as a function of concentration of Photoflo 600**

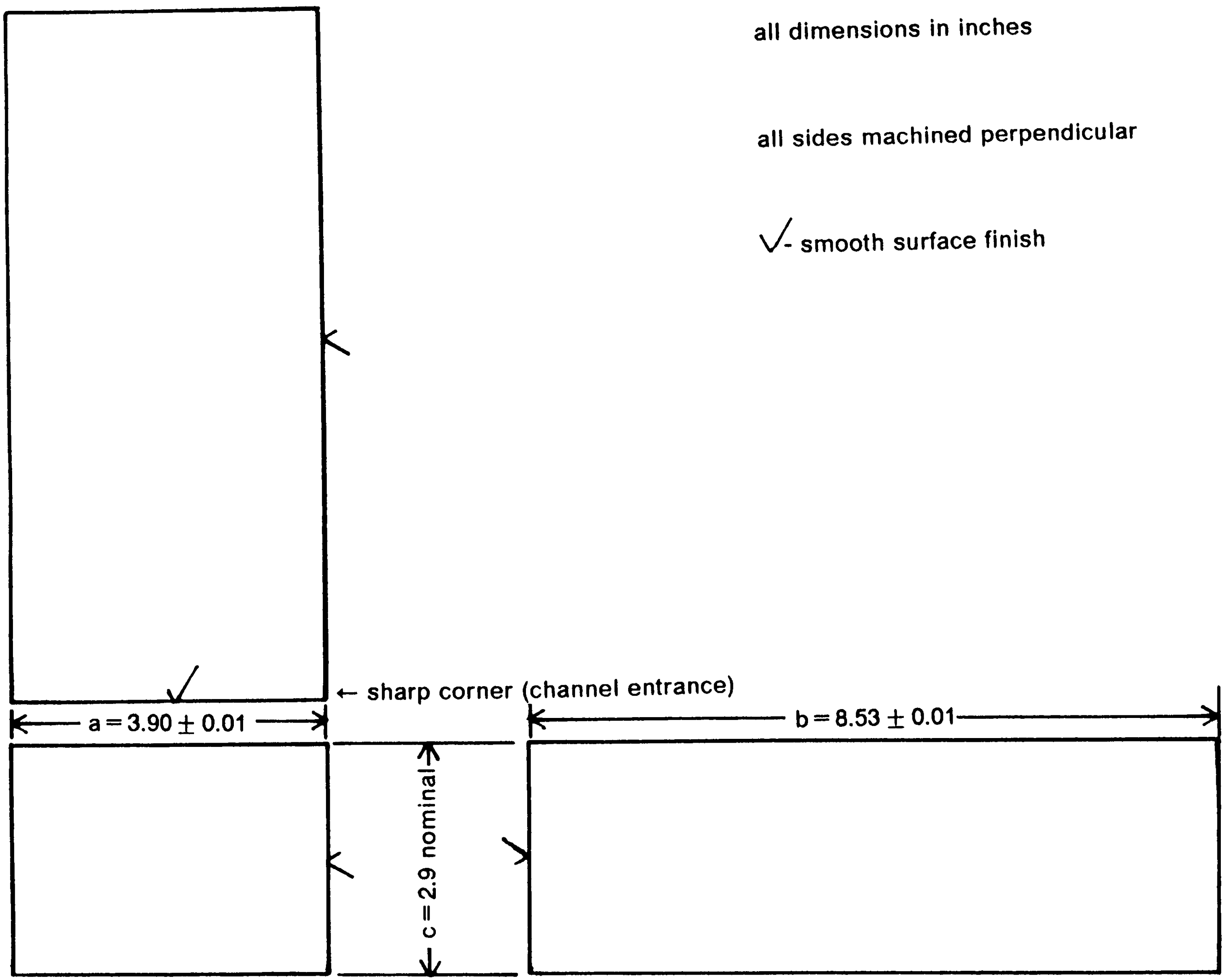

Figure 24. Shop drawing of aluminum block used in test section.

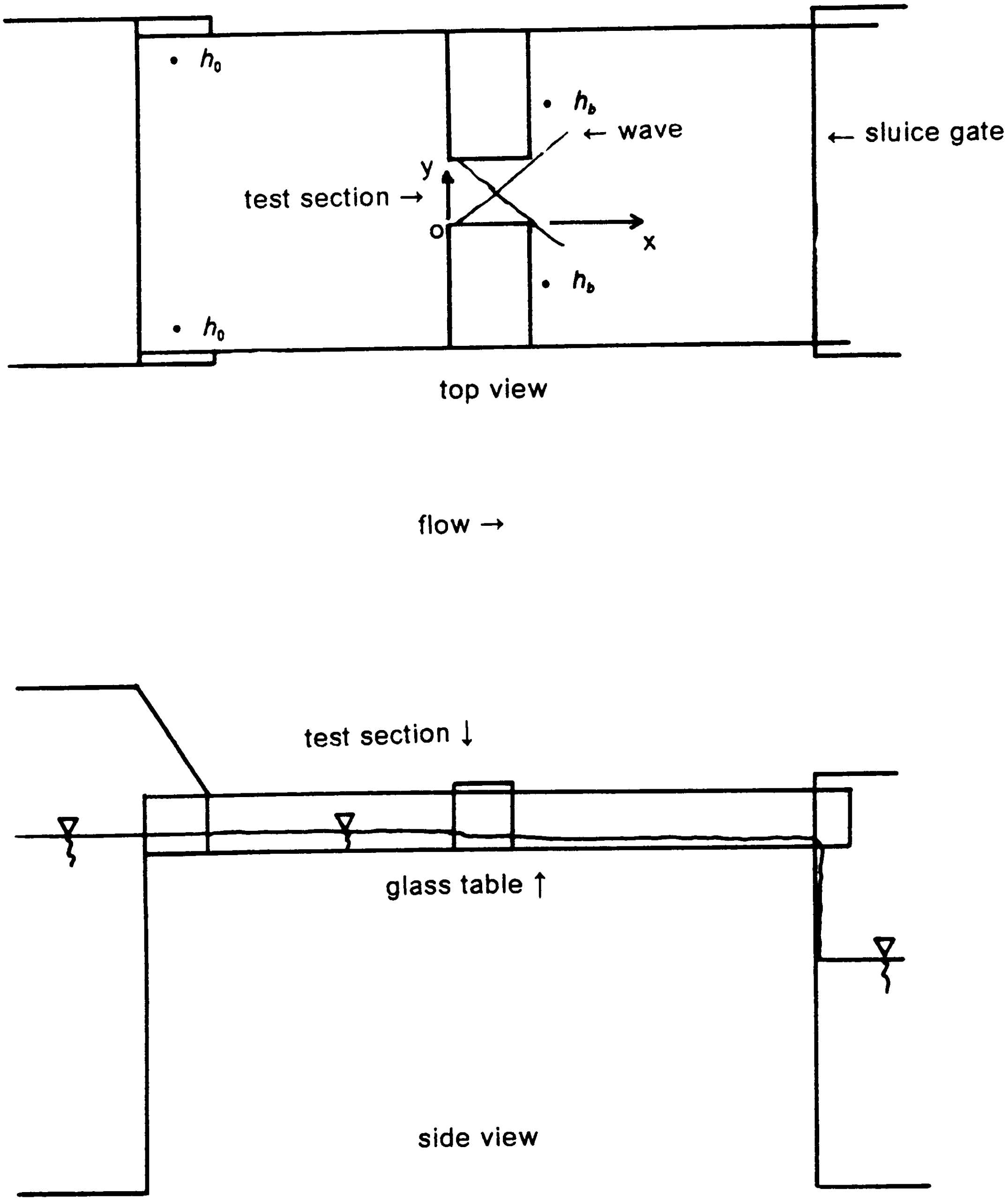

Figure 25. Representative test section and flow regime

In all, five test cases were performed. These are summarized in Fig. 26, labeled as cases A through E. There are two basic configurations which can be seen in Fig. 26, symmetrical and one-sided. For the symmetrical configurations, cases B and C, the blocks were placed as shown in the example of Fig. 25. In doing so, a tip gap with an inviscid shroud wall and its mirror image are modeled. To obtain the one-sided case, cases A, D and E, a strip of stainless steel sheet metal was placed along the length of the water table to give the proper channel width. In this case, the tip gap and shroud wall are modeled.

Also seen in Fig. 26, two channel length to half-width $\left(\frac{l}{w}\right)$ ratios were chosen to provide different geometries. Cases A, B, and C all have $\frac{l}{w} = 2.6$, but each has a different half-width, w. In this way, the effect of scaling on the flow can be examined. Configurations D and E have $\frac{l}{w} = 1.32$ and the same half-width, but different overall height ratios, $\frac{h_b}{h_0}$. Thus, the effect of $\frac{h_b}{h_0}$ ($\sqrt{\frac{P_b}{P_0}}$ by the hydraulic analogy) can be investigated. In addition, configurations A and D can be compared to examine the effect of geometry on the flow. Both have similar half-widths and $\frac{h_b}{h_0}$, but each has a different $\frac{l}{w}$.

The locations for the measurement of h_0 and h_b are shown in the sample configuration in Fig. 25. For each case, h_0 was measured as far upstream and off center as the traversing mechanism would allow. In the case of a symmetrical configuration like the one shown in Fig. 25, an average of the heights on either side of center upstream was used. The downstream height, h_b, was measured far enough downstream and to the side to avoid interference with the jet at the channel exit and the meniscus along the sides of the block and the water table side walls. For the five cases run, h_b was taken at about 2.5 cm downstream of the exit and 12.7 cm from the centerline.

test configuration	$\frac{l}{w}$	half-width w (m)	$\left(\frac{h_b}{h_0}\right)^2$
A	2.6	0.0762	0.0384
B	2.6	0.0381	0.038
C	2.6	0.0293	0.038
D	1.32	0.0749	0.0397
E	1.32	0.0749	0.181

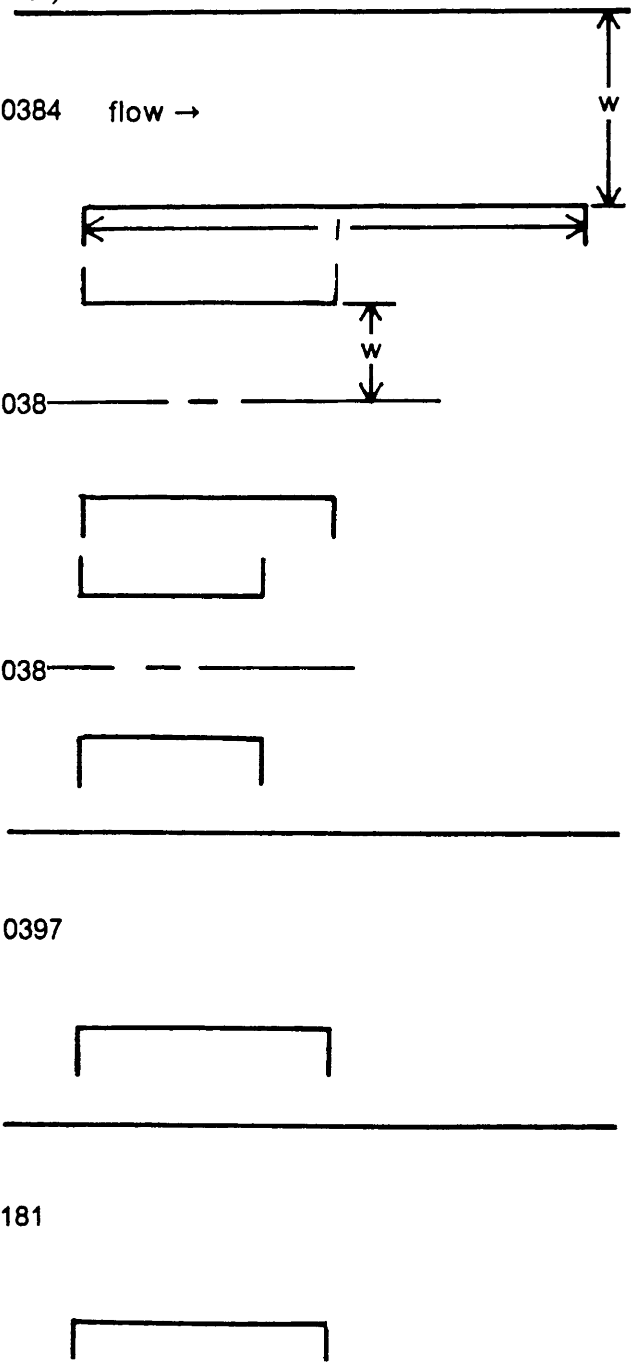

Figure 26. Test section configurations

Again, for symmetrical cases, an average value of heights at locations equidistant from the channel centerline at a fixed downstream location was used.

Three criteria were used in choosing values for h_0 and h_b. First, h_0 was chosen such that the depth of water in the channel would be in the range of 0.5 to 1.0 cm, where the hydraulic analogy would hold best. It was decided to choose h_b very low to give high Froude numbers and stronger hydraulic jumps. Finally, h_0 and h_b were selected to give overall height ratios, $\frac{h_b}{h_0}$, which would yield pressure ratios similar to those used by Norwood [12]. During the course of each test, h_0 remained constant to within 0.002 in (0.05 mm).

For each test a set of water heights upstream and in the channel was taken. Moving along a line at a fixed distance from the channel wall, a fixed y value, surface height measurements were taken at points along the direction of flow (in the positive x direction). This was done across the entire channel half-width, creating a grid of water heights which can then be easily converted to a grid of height ratios, $\frac{h}{h_0}$, for use in data analysis.

Chapter IV

Experimental Results

Major Features of Channel Flow

Flow observed on the water table is shown schematically in Fig. 27. The figure shows one-half of the symmetrical channel flow with the direction of flow from left to right. Starting from h_0, the flow accelerates from subcritical ($F < 1$, $\frac{h}{h_0} > \frac{2}{3}$) to critical ($F = 1$, $\frac{h}{h_0} = \frac{2}{3}$). As seen from the shape of the line of critical flow in Fig. 27, the flow accelerates more rapidly near the corner of the channel. The flow then remains supercritical ($F > 1$, $\frac{h}{h_0} < \frac{2}{3}$) throughout the rest of the channel.

Associated with the rapid acceleration of the flow around the corner of the channel entrance is a location of minimum water height, h_σ. The location of minimum height appears as a dimple in the water surface. This dimple is the beginning of a trough

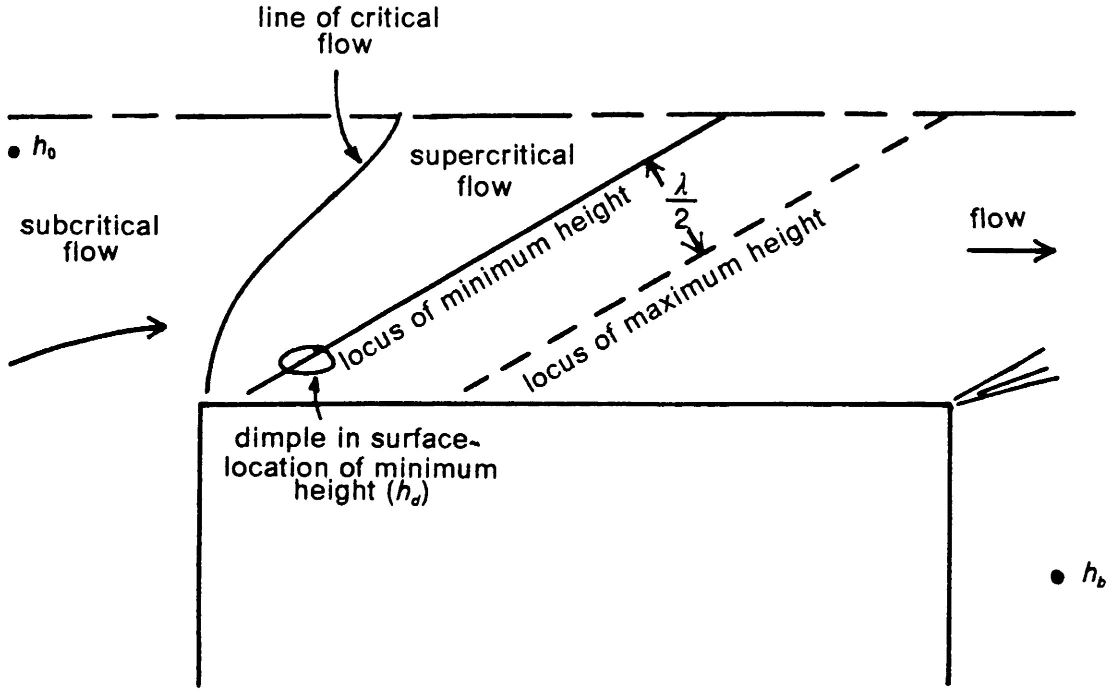

Figure 27. Schematic of flow in the water channel

or line of minimum water height which extends to the centerline, gradually becoming less sharp.

The trough described above is the beginning of an oblique hydraulic jump which is shown in Fig. 27. This jump results from the turning of the flow as it accelerates around the corner. The distance measured perpendicularly from the trough to the line labeled locus of maximum height corresponds to one-half of the wavelength $\left(\frac{\lambda}{2}\right)$ of the hydraulic jump.

The flow then exits the channel and expands to the downstream water height, h_b. At the corner of the channel exit, an expansion fan is present, as seen in Fig. 27.

Test Results

The results of the five test cases are presented here. First, the results of the basic configuration, case B in Fig. 26, are presented along with the analysis used to obtain the results. Then, the corresponding results for the other four cases will be presented.

As seen from case B in Fig. 26, the basic configuration was symmetrical with $\left(\frac{h_b}{h_0}\right)^2 = 0.038$. Surface height measurements were taken and a contour plot of $\frac{h}{h_0}$ was prepared. This plot, along with a plot of corresponding Froude numbers appears in Fig. 28. Note the regions of flow in Fig. 28 correspond to those described in the flow schematic of Fig. 27. The flow accelerates from rest through the subcritical range to critical flow at $\frac{h}{h_0} = \frac{2}{3}$ or $F = 1$. The region of flow following the line of critical flow remains supercritical with $\frac{h}{h_0} < \frac{2}{3}$ and $F > 1$.

Figure 28 also shows the rapid acceleration of the flow around the corner with a dimple occurring at x=1.14 cm, y=0.38 cm. The height ratio at this point is $\frac{h_d}{h_0} = 0.394$. Associated with this minimum height ratio is a maximum or dimple Froude number, F_d. For this case, $\frac{h_d}{h_0} = 0.394$ yields $F_d = 1.75$.

The hydraulic jump discussed for the schematic of Fig. 27 was seen to exist in all the test cases. In order to compare the jumps observed in each case, the hydraulic jump relations developed in Appendix A are used to determine the strength and angle of each wave. The analysis used is presented below, with reference to the schematics shown in Figs. 29 and 30. Figure 29 shows the definitions of the water heights used to determine the relative strength of the wave, while Fig. 30 shows the terminology used to find the angle of the wave.

As Fig. 29 shows, the minimum water height, h_d, is defined as h_1, or the water height just before the hydraulic jump. The height just after the hydraulic jump, h_2, is defined as the maximum height the water reaches along the line $y = y_d$, where y_d is the y coordinate of the dimple. In doing so, the ratio $\frac{h_2}{h_1}$, a measure of the strength of the hydraulic jump, can be found.

For comparison, a method was developed for predicting the angle of the wave from the measured surface heights. This is based on the conceptual model of free streamline flow intersecting a wall. Figure 30 shows this schematically. In examining the data, it is helpful to note the location on the channel wall where the oblique wave forms. This location was estimated from the contour plots of Figs. 28 and 31-34. An

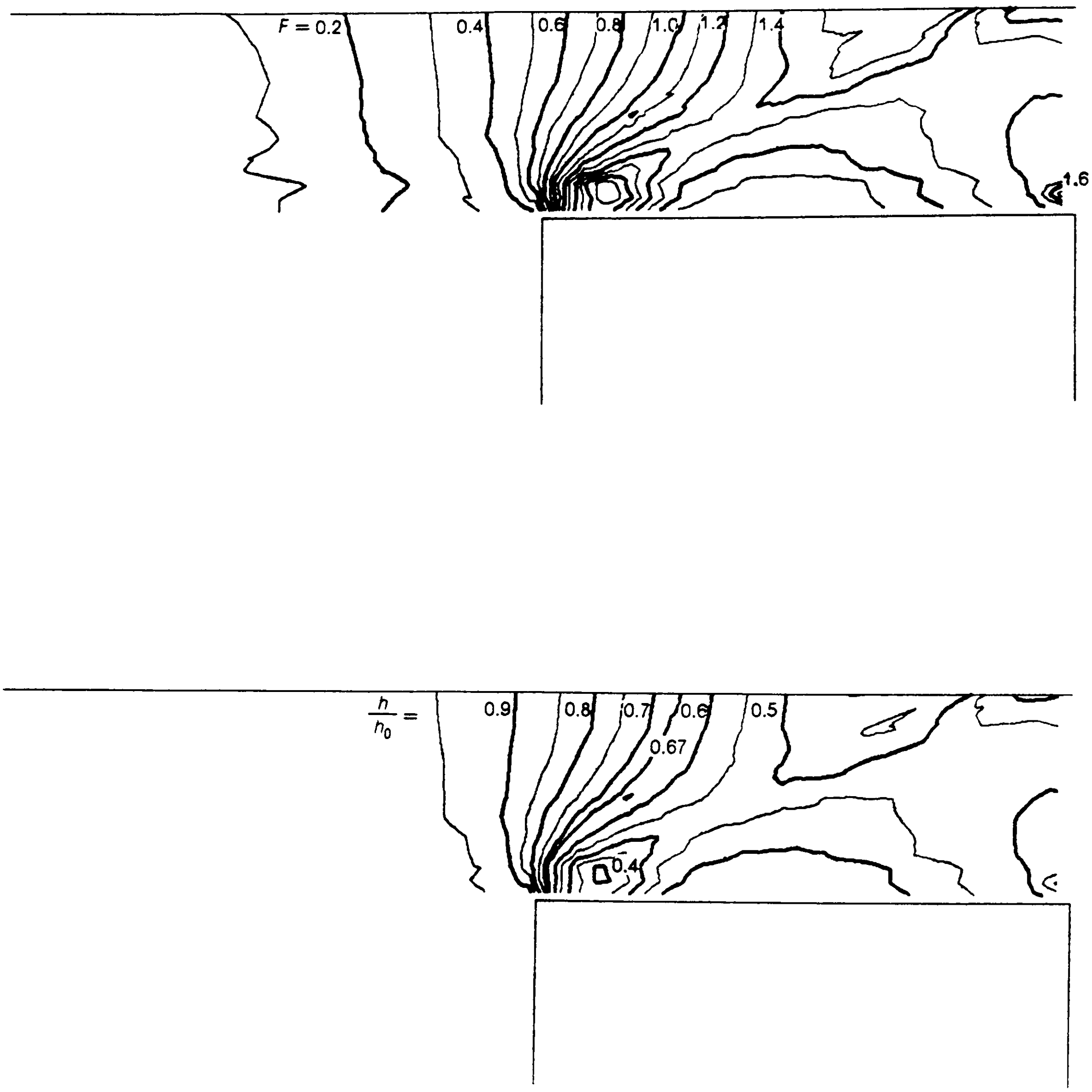

Figure 28. Contours of Froude number and height ratio, case B

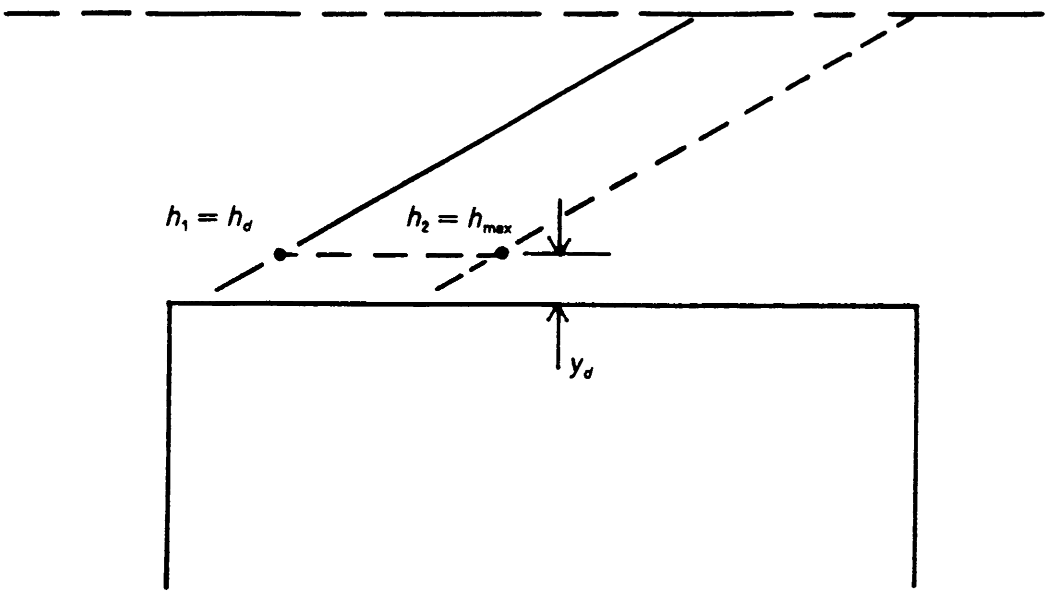

Figure 29. Quantities used to determine strength of jump

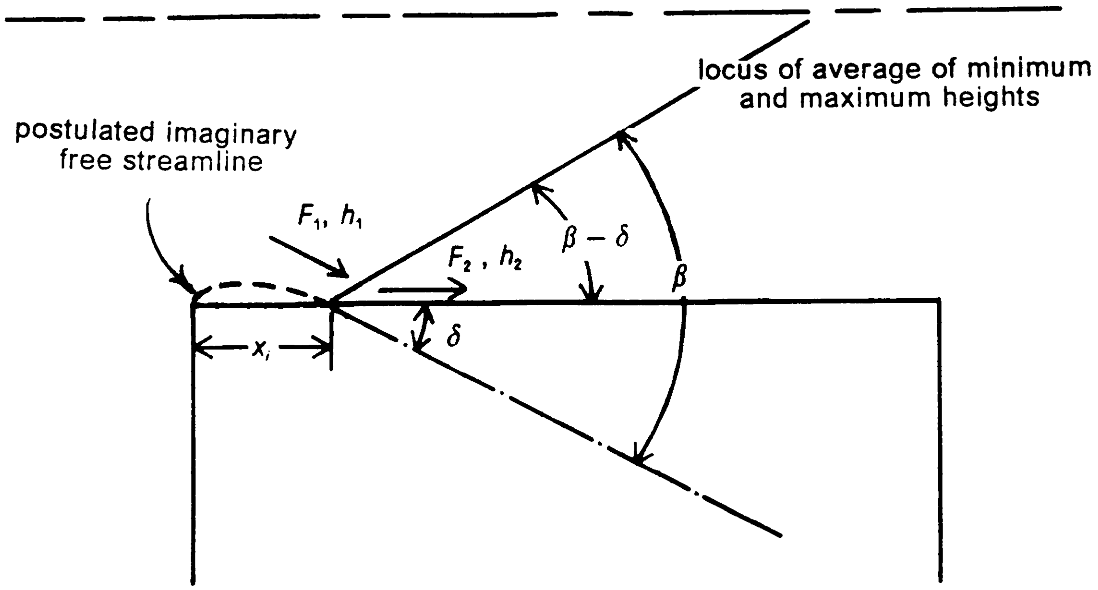

Figure 30. Quantities used to determine jump angle

average of the loci of maximum and minimum heights was drawn. The point were this median line intersects the channel wall is then considered the location of the wave formation. The distance from the channel entrance to this point of intersection, x_i, is as shown in Fig. 30. It is the point where the "free streamline" contacts the wall causing the flow to turn.

To calculate the angle of the wave, the following equations from Appendix A are used in reference to Fig. 30:

$$F_1 = \sqrt{2\left(\frac{h_0}{h_1} - 1\right)}$$

$$\sin\beta = \frac{1}{F_1}\sqrt{\frac{1}{2}\frac{h_2}{h_1}\left(\frac{h_2}{h_1} + 1\right)}$$

$$\tan(\beta - \delta) = \frac{\tan\beta}{\left(\frac{h_2}{h_1}\right)}$$

As the flow accelerates around the corner, the "free streamline" will intersect the channel wall at an angle δ. The wall then turns the flow through this angle, resulting in an oblique hydraulic jump which makes an angle β with the direction of incoming flow. The angle $\beta - \delta$ is the angle between the jump and the channel wall. This angle was measured from the data as the angle with which the locus of average heights intersects the channel sidewall.

For the basic configuration, case B,

$$\frac{h_1}{h_0} = \frac{h_d}{h_0} = 0.394 \text{ and } \frac{h_2}{h_0} = 0.651$$

resulting in

$$\frac{h_2}{h_1} = 1.65.$$

Using these values in the above equations yields

$$F_1 = \sqrt{2\left(\frac{1}{0.394} - 1\right)} = 1.75,$$

$$\sin\beta = \frac{1}{1.75}\sqrt{\frac{1}{2}(1.65)(1.65 + 1)} = 0.845$$

$$\beta = 57.7°$$

$$\tan(\beta - \delta) = \frac{\tan(57.7)}{1.65} = 0.957$$

$$\beta - \delta = 43.8°$$

resulting in

$$\delta = 13.9°.$$

The measured angle, $\beta - \delta$, obtained in this case is 31°.

The other four cases were treated in a similar manner. The contour plots of $\frac{h}{h_0}$ and F appear in Figs. 31-34. Calculations were performed for all cases as above. The results of these calculations and the corresponding measurements are summarized in Table 2. The final column of Table 2 shows the measured value of wavelength, expressed in channel half-widths, $\frac{\lambda}{w}$.

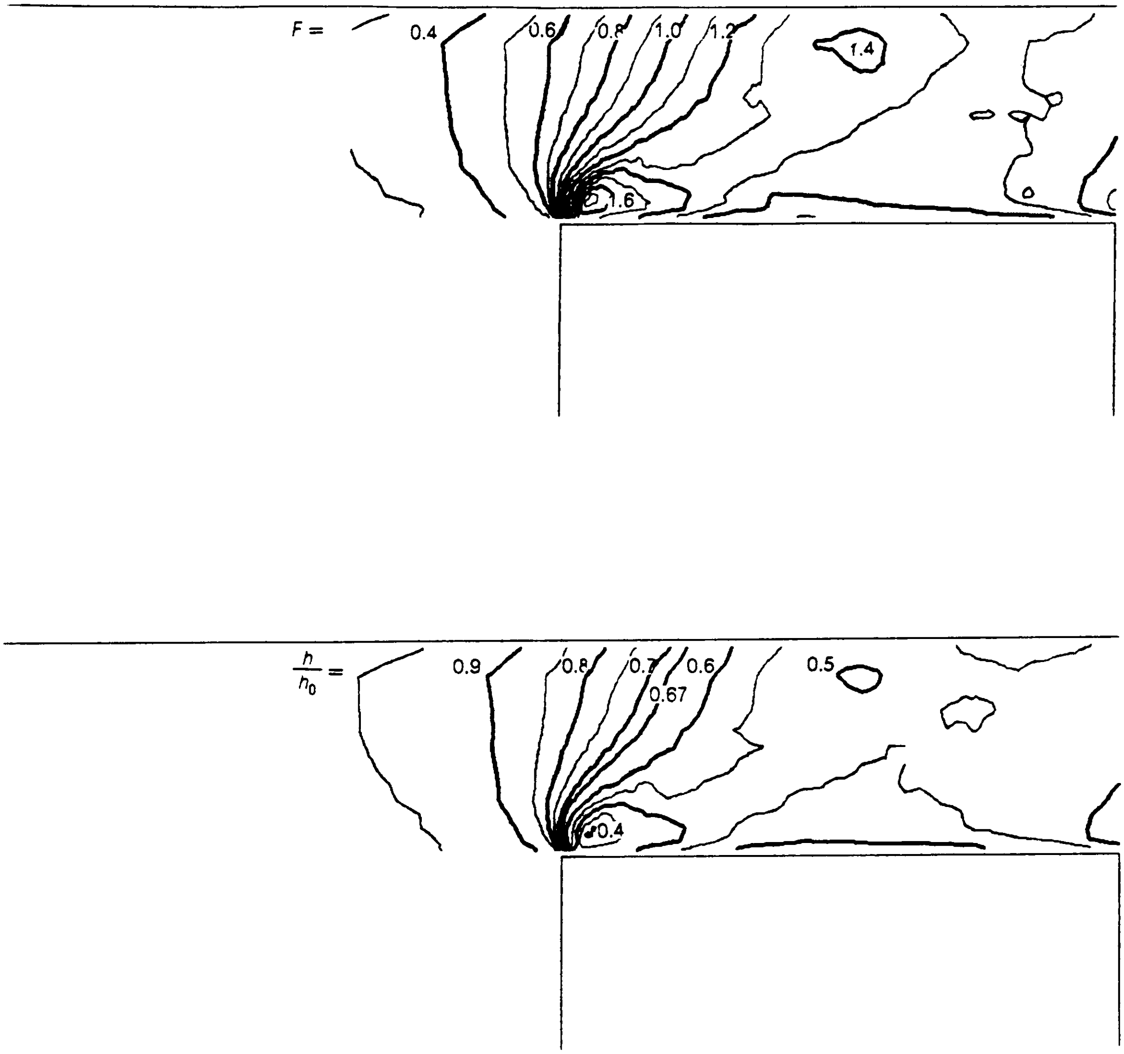

Figure 31. Contours of Froude number and height ratio, case A

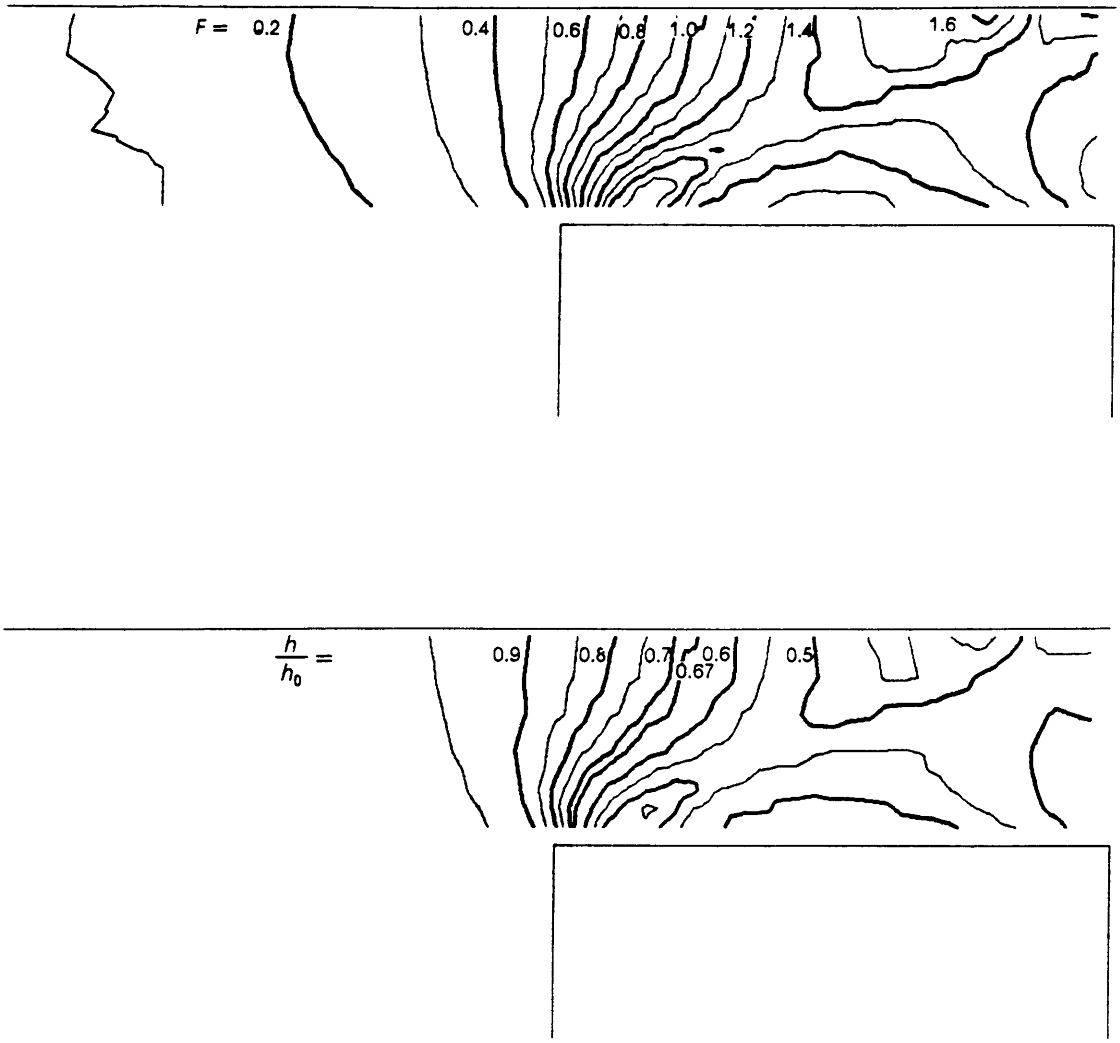

Figure 32. Contours of Froude number and height ratio, case C

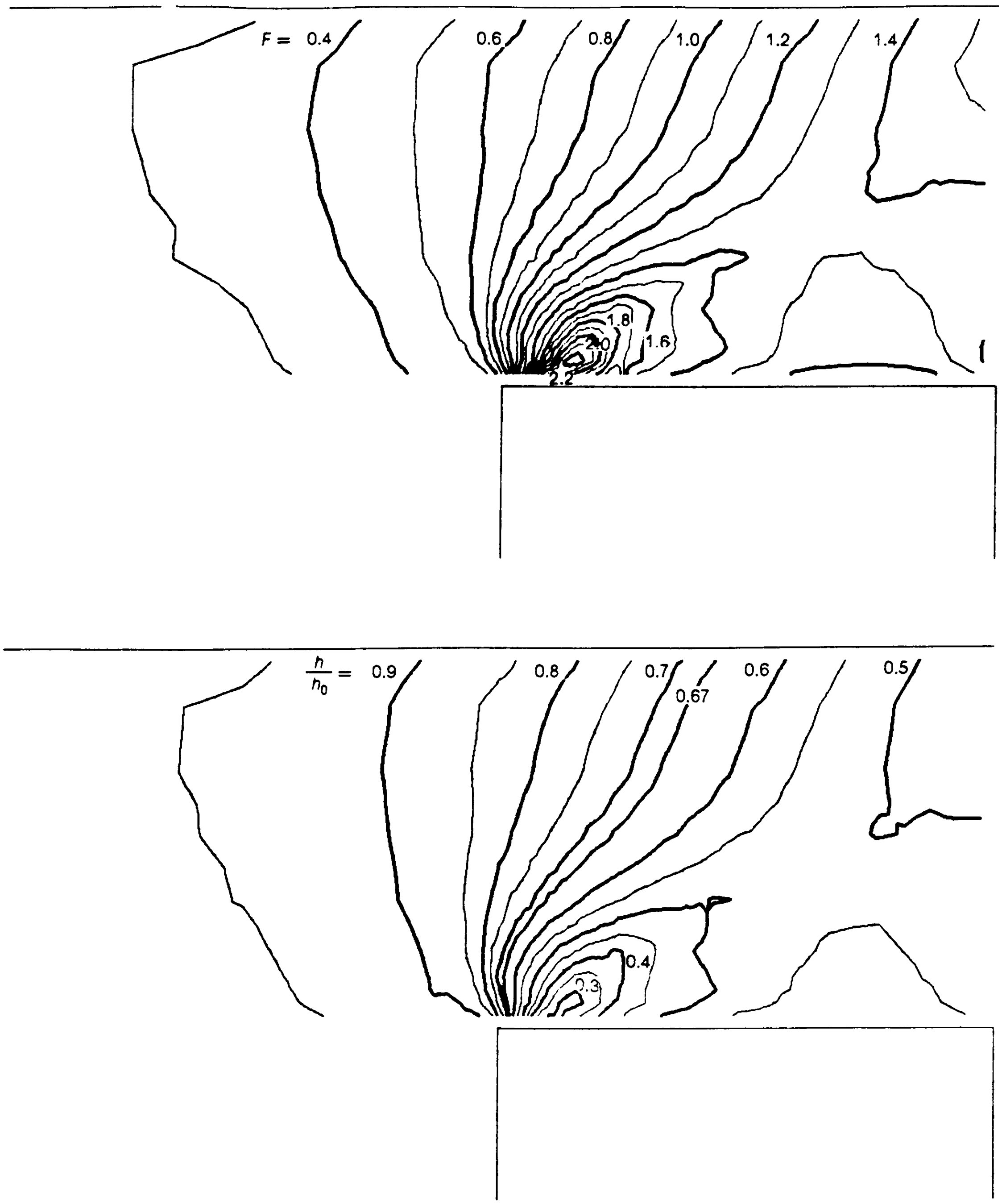

Figure 33. Contours of Froude number and height ratio, case D

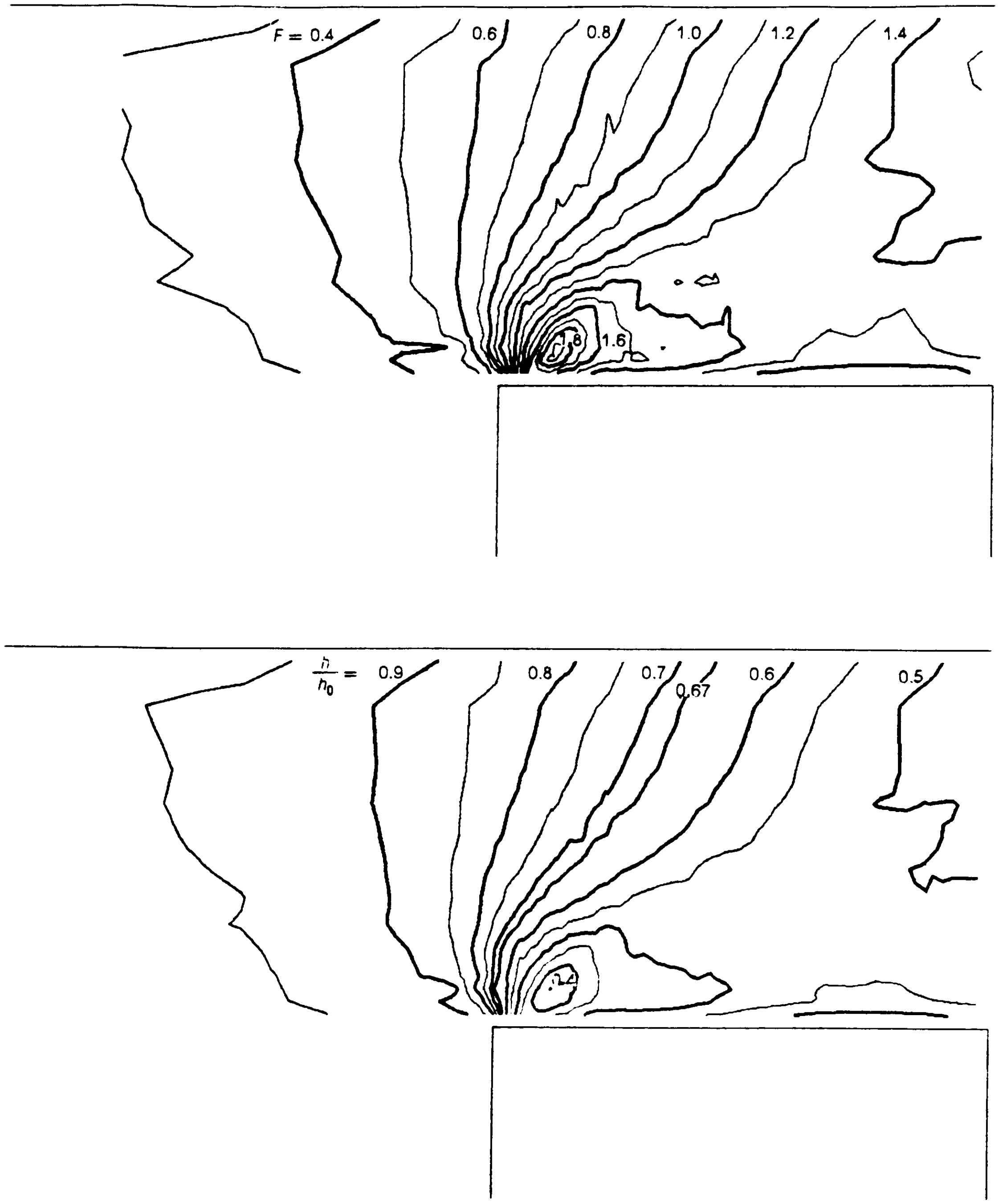

Figure 34. Contours of Froude number and height ratio, case E

Table 2. Summary of water table results

test config.	$\frac{l}{w}$	half-width w (m)	$\left(\frac{h_b}{h_0}\right)^2$	$\frac{h_d}{h_0}$	F_d	$\beta - \delta°$		$\frac{\lambda}{w}$
						calc.	meas.	
A	2.6	0.0762	0.0384	0.395	1.75	40	37	0.84
B	2.6	0.0381	0.038	0.394	1.75	44	31	0.89
C	2.6	0.0293	0.038	0.439	1.60	45	31	1.02
A	2.6	0.0762	0.0384	0.395	1.75	40	37	0.84
D	1.32	0.0749	0.0397	0.276	2.29	31	35	0.83
E	1.32	0.0749	0.181	0.349	1.93	35	28	0.50

For ease of comparison, the results are tabulated in two groups; A, B, C and A, D, E. Cases A, B, and C are grouped to examine the effect of scaling; all three have the same $\frac{h_b}{h_0}$ and $\frac{l}{w}$ but different half widths, w. The second grouping, A, D, E all have similar w and can further be divided to examine the effect of geometry and overall height ratio, $\frac{h_b}{h_0}$. Cases A and D have different $\frac{l}{w}$ and can therefore be examined to study the effect of geometry on the flow. Finally, by looking at cases D and E, the effect of $\frac{h_b}{h_0}$ can be studied, since both differ only in the overall height ratio.

Chapter V

Discussion of Results

The results presented in the previous chapter are discussed here. First, the effects of three parameters--scaling, geometry, and overall water height ratio--on dimple Froude number will be examined. Then, an examination of the line of critical flow and oblique wave structure will be presented. The results of applying the modified hydraulic analogy to the data are then compared to available data and calculations for compressible flow through sharp-edged orifices.

Dimple Froude number

The results for cases A, B, and C shown in Table 2 demonstrate the effect scaling has on the maximum or dimple Froude number, F_d. All three have the same geometry, $\frac{l}{w} = 2.6$, and an overall water height ratio of about $\frac{h_b}{h_0} = 0.195$. However, each case has a different half-width, w. For case A, w=0.0762 m, for case B, w=0.0381 m, and for case C, w=0.0293 m. The results show that as the scale is decreased, the maximum Froude number decreases. Case C, which is 76.9 percent scale of the basic configuration case B, has a $F_d = 1.6$, while case B has $F_d = 1.75$. Case A, which is twice the scale of case B, shows $F_d = 1.75$, the same as case B.

The reason for F_d of case A being equal to that of case B may be twofold. First is the way the configuration was set up on the water table. Cases B and C were symmetrical, they had an inviscid centerline. Case A, however, had for its centerline a piece of sheet metal. Friction along this centerline would cause flow blockage and this may have contributed to a lower dimple Froude number. Secondly, the models in cases A and B may be large enough for the effect of scaling to be negligible. As a result, no appreciable change in F_d is observed when increasing the model scale.

Comparing cases A and D demonstrates the effect of geometry on F_d. Both these cases have similar half widths, 0.0762 m for case A and 0.0749 for case D, and overall height ratios, 0.0384 and 0.0397 respectively. The main difference is the geometry. Case A has $\frac{l}{w} = 2.6$ and case D has $\frac{l}{w} = 1.32$. The resulting dimple Froude numbers are $F_d = 1.75$ for case A and $F_d = 2.29$ for case D. Thus reducing the length relative to the width increases the dimple or maximum Froude number.

The effect of overall height ratio, $\frac{h_b}{h_0}$, is seen by examining cases D and E. Both these cases have the same $\frac{l}{w} = 1.32$, the same w=0.0749 m and both have a sheet metal wall along the centerline. In comparing these two cases, it is seen that lowering $\frac{h_b}{h_0}$ results in a higher F_d. With $\frac{h_b}{h_0} = 0.199$, for case D, $F_d = 2.29$, while when $\frac{h_b}{h_0} = 0.425$ in case E, $F_d = 1.93$. There is a more rapid expansion of the flow around the corner for a lower overall height ratio than for a higher one.

Shape and location of F=1 line

The shape of the line of critical flow (F = 1) for all cases is similar to the shape of the sonic line (M = 1) in Fig. 19. The critical flow line moves slightly upstream before curving downstream. Also, the F = 1 lines intersect the channel centerline at nearly an angle of 90°.

Unlike the sonic lines of Fig. 19, the F = 1 lines do not begin at the channel entrance. Instead, they begin slightly downstream of the channel entrance. Table 3 below shows the location of the start of the F = 1 lines for each case.

Table 3. Sidewall location of F = 1 line

configuration	$\frac{l}{w}$	half-width (m)	$\left(\frac{h_b}{h_0}\right)^2$	distance, $\frac{x}{w}$, half-widths
A	2.6	0.0762	0.0384	0.028
B	2.6	0.0381	0.038	0.061
C	2.6	0.0293	0.038	0.094
A	2.6	0.0762	0.0384	0.028
D	1.32	0.0749	0.0397	0.031
E	1.32	0.0749	0.181	0.025

The above results show that scaling has the only appreciable effect on the start of the F = 1 line. As the overall scale of the channel increases, the line of critical flow starts closer and closer to the channel entrance; it moves from x = 0.094w for case C to x = 0.028 w for case A. Comparing cases A, D, and E, the results are equal within experimental error and therefore any effect of model geometry or overall height ratio is not readily visible.

Figure 35 shows a plot of the distance in half-widths from the orifice entrance to the intersection of the sonic line with the orifice centerline against the freestream Mach number for Norwood's data of Fig. 19. This shows that as the freestream Mach number is increased from 1, the sonic line goes from parallel to the centerline to intersecting the centerline at $\frac{x}{w} = 0.433$ for the limiting case of choked flow.

Also in Fig. 35 the distances from the channel entrance to the intersection of the F = 1 line with the centerline are plotted against dimple Froude number. The dashed lines in Fig. 35 are the curves obtained by shifting the curve for Norwood's data up 0.1w and 0.2w respectively. In doing so, it is seen that the data for the test cases differs from Norwood's data by 0.16 w ± 0.05 w The error analysis in Appendix C indicates that the error in location of the F = 1 lines is ± 0.05 w. This would imply that the + 0.16w observed in Fig. 35 is a real phenomenon.

There are four possible explanations for the + 0.16w difference observed in Fig. 35. First is the delay in the start of the F = 1 line observed in Table 3. With the F = 1 line starting farther downstream, its intersection with the centerline would be expected to occur farther downstream also. Next, is the assumption of the hydraulic analogy that the $V = \sqrt{gh}$. It may be that the faster capillary waves are interfering with the measurements. Standing capillary waves would result in higher surface height measurements, or lower Froude numbers. Thus, the line of F = 1 would occur farther downstream. Thirdly there are the viscous effects of the channel sidewall and bottom wall. Viscosity would slow the fluid, causing F = 1 to occur farther downstream. Finally, since the hydraulic analogy is for a gas of k = 2, part of the difference may come in comparison with calculations for a gas with k = 1.4.

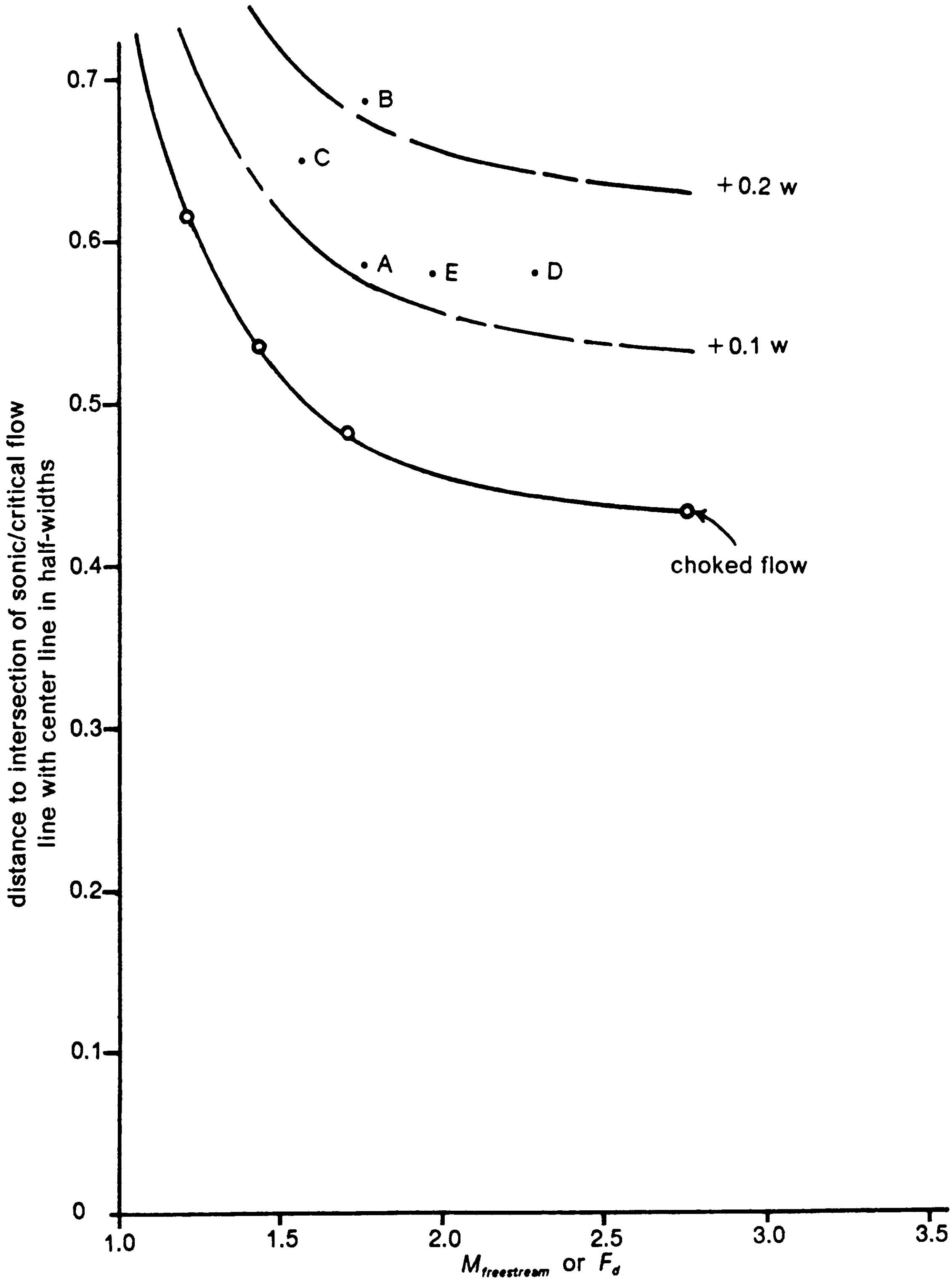

Figure 35. Comparison of F=1 lines and sonic lines of Norwood

Effective wall location of wave formation

From the free streamline data of Benson and Pool and Norwood, Fig. 36 was constructed. This figure shows the distance from the orifice entrance to the point of intersection of the free streamline with a line drawn from the orifice edge parallel to the orifice centerline (x_i) plotted against the freestream Mach number. This distance is plotted as $\frac{x_i}{w}$, or the distance in half orifice widths. The figure shows that at higher Mach numbers, the free streamline intersects the "wall" closer to the orifice edge. As the Mach number decreases, the free streamline intersects the wall farther and farther downstream. The free streamline becomes parallel to the wall at a pressure ratio of 0.425 or $M = 1.18$ as indicated by Benson and Pool.

Figure 36 also plots the data for the five water table cases against dimple Froude number. Two points are plotted for each case, the location of the intersection of the line of median heights with the channel wall, denoted by the symbol m, and the location of the intersection of the line of maximum heights with the channel wall, denoted by the symbol p. In four of the five cases, A, B, D, and E, the median and maximum points straddle the curve of Fig. 36. Point C however does not. This may be due to the scale effect on the dimple Froude number. Comparing cases A and D shows that case D with the lower $\frac{l}{w} = 1.32$ has a shorter $\frac{x_i}{w}$ than case A which has $\frac{l}{w} = 2.6$. The effect of overall height ratios is also evident. Case D with the higher $F_d = 2.29$ has a shorter $\frac{x_i}{w}$ than case E with $F_d = 1.93$.

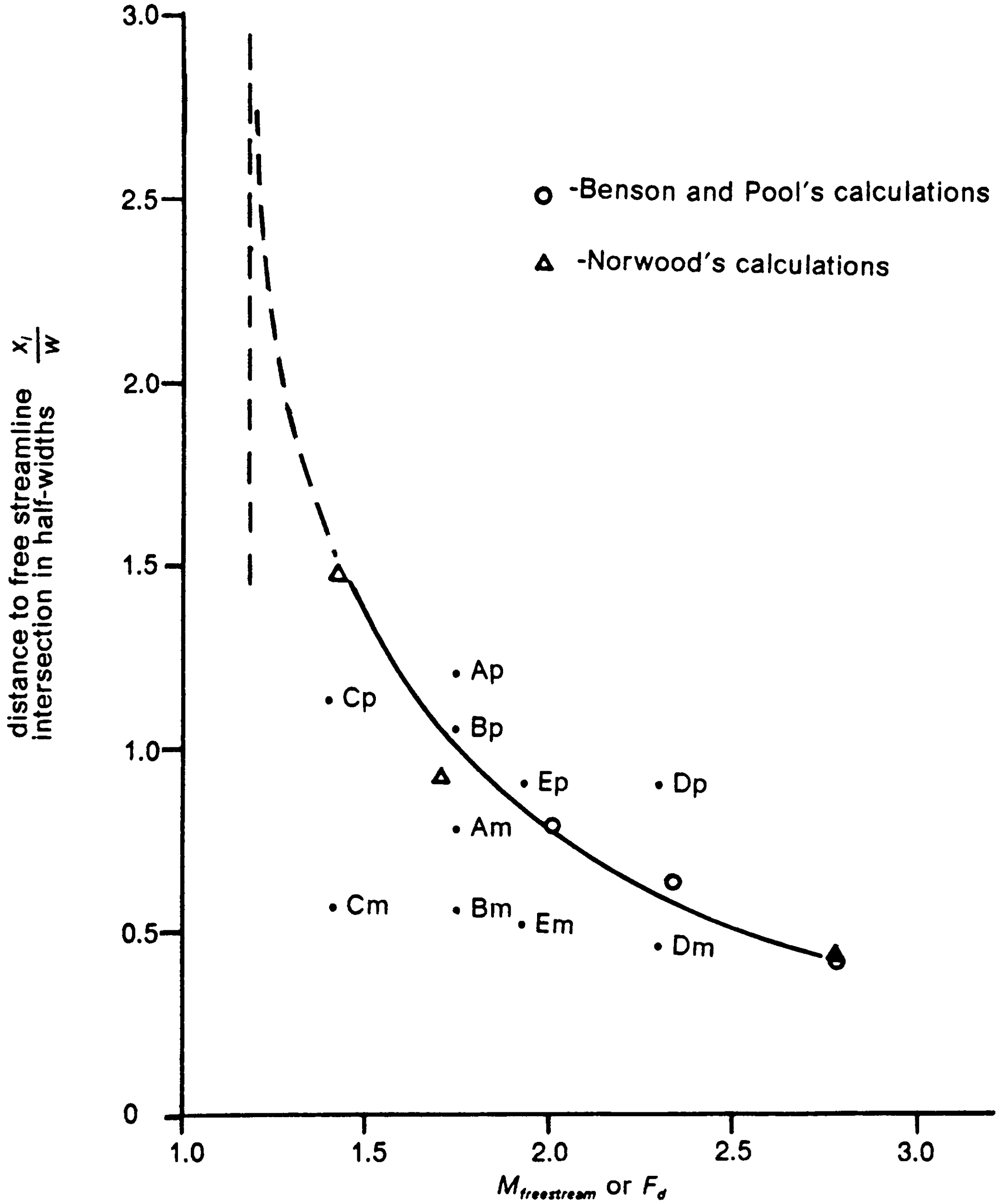

Figure 36. Comparison of free streamline intersection

Wave angles

The measured angles of the wave relative to the channel sidewall as shown in Table 2 for cases A through E are 37, 31, 31, 35, and 28 degrees respectively. The angles calculated using the data and classical hydraulic theory were 40, 44, 45, 31, and 35 degrees respectively. Since the values of the data used in the classical theory were estimates limited by the physical set up of the test sections, some difference is to be expected.

Suggested model for wave formation

From the above discussion, it is seen that an oblique wave or hydraulic jump does form in the water channel. As the flow accelerates around the corner of the channel entrance, the "free streamline" contacts the channel wall, causing an abrupt change in the direction of flow. In the cases tested, the flow expanded around the corner reaching maximum Froude numbers of 1.6 to 2.3. The flow behaved as if a free streamline intersected the channel sidewall within 1.5 half widths. At this point, the flow was turned through an angle of ten to 20 degrees by the wall resulting in the formation of weak waves at an angle to the channel wall of 28 to 36 degrees. The measured wavelengths in Table 2 show that for given flow conditions, wavelength varies as channel half-width. For cases A through D, with $\left(\frac{h_b}{h_0}\right) = 0.038$, the wavelength expressed in half-widths remains approximately constant, about

$\frac{\lambda}{w} = 0.9$. This agrees with Laitone's observation that a larger model will give larger wavelengths, thus reducing the effects of capillary waves.

Free stream turning angles for compressible gas flows

As it has been demonstrated by the model that the flow is turned as it intersects the channel wall, application of the model to compressible gas flows is the next logical step. In order to apply the water table results to a compressible gas flow, the modified hydraulic analogy was applied. Using the calculated values of $\frac{h_2}{h_1}$ as $\frac{\rho_2}{\rho_1}$ in the gas dynamics equations of Appendix A with $k = 1.4$, turning angles, δ, were calculated for each of the five test cases. These results were compared with the results of Norwood.

The free streamline data of Norwood found in Fig. 20 was used to construct Fig. 37. Figure 37 shows the angle of turn, δ, (or equivalently the angle with which the free streamline intersects the wall) plotted against the free stream Mach number. This shows that for low Mach numbers, the free streamline intersects the wall at small angles. The angle of intersection becomes steeper as the Mach number increases. As in Fig. 36, the minimum M for which the flow would intersect the wall is 1.18. Also shown in Fig 37 is the line of minimum M required for an attached shock for a given δ. It is interesting to note that for $M < 1.75$, Norwood's data follows this very closely. It would appear that this would imply that the shock formation is like that of an attached shock on a wedge of half-angle δ .

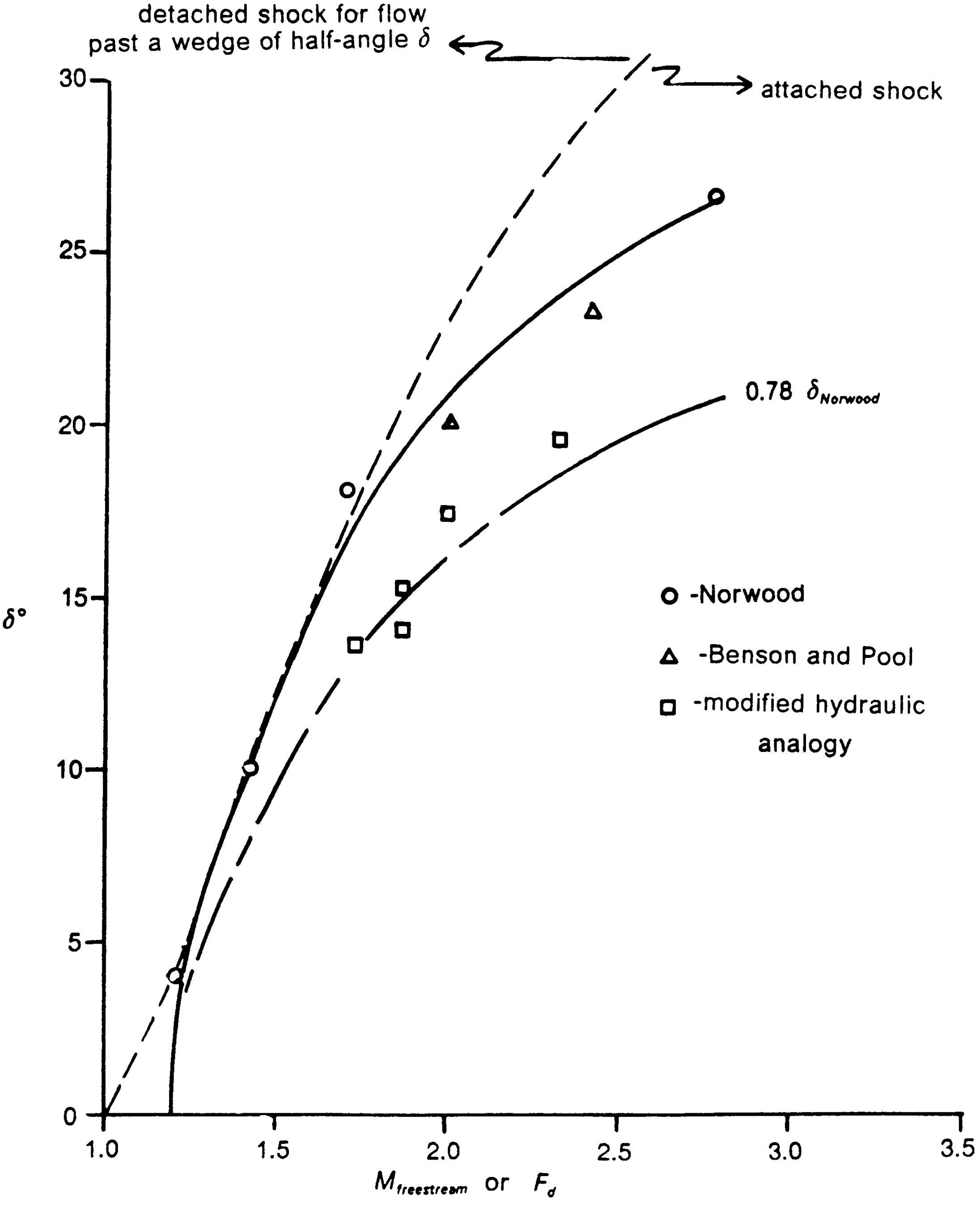

Figure 37. Compressible flow turning angles

The five turning angles calculated using the hydraulic analogy are also plotted in Fig. 37 against the isentropic Mach number based on the dimple height ratio, M_d. These results predict a turning angle 78 ± 5 percent of the turning angle predicted by Norwood's orifice flow calculations. One would expect the addition of walls to a sharp-edged orifice to affect the flow in such a way that the expansion would be slower and the turning angle would therefore be smaller. However, the magnitude of this difference is not known.

Analogous wave formation in compressible flows

To show an event similar to the one discussed above for compressible gas flows, an example is worked out here using one of Norwood's cases. For the case of $\frac{p}{p_0} = 0.039$, the orifice with an imaginary wall is sketched in Fig. 38a to a scale similar to the basic configuration, case B. As the flow comes around the corner, the free streamline intersects the wall at an angle of $\delta = 26.5°$ measured from Norwood's free streamline calculations shown in Fig. 20. For this pressure ratio, an isentropic Mach number $M = 2.757$ is obtained. Using this δ and M in the compressible flow relations developed in Appendix A, a shock angle can be calculated. For this case, the shock angle $\sigma = 46.7°$ is obtained for the weak case and $\sigma = 78°$ for the strong case. Based on the relative magnitudes of the wave angles observed on the water table, the results for the weak case are sketched in Fig. 38a.

Since the modified hydraulic analogy data would indicate a smaller turning angle than expected for a sharp-edged orifice, Fig. 38b was prepared using the δ value predicted

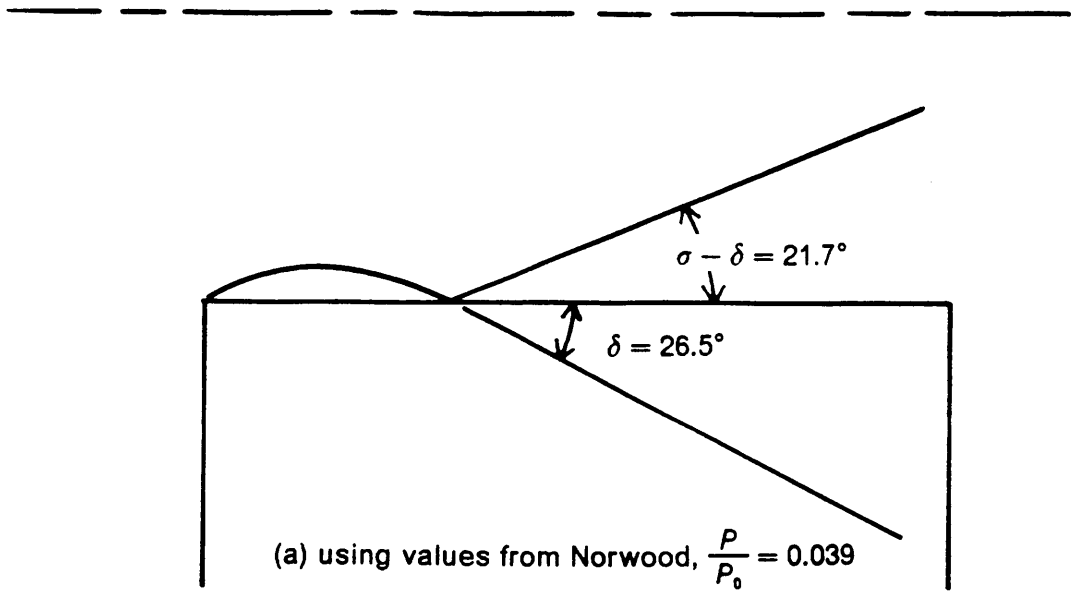

(a) using values from Norwood, $\frac{P}{P_0} = 0.039$

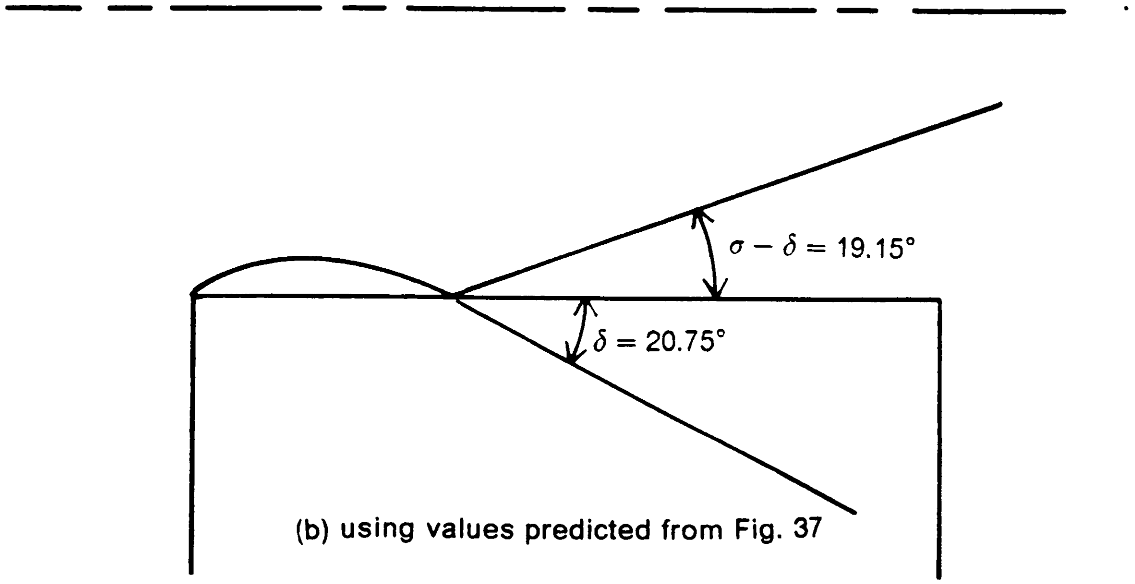

(b) using values predicted from Fig. 37

Figure 38. Shock formation in compressible gas flow

by Fig. 37. For the same isentropic Mach number, $M = 2.757$, the modified analogy would predict $\delta = 20.75°$. Using these values in the appropriate compressible flow equations yields $\sigma = 39.9°$.

Implications for jet engine heat transfer

The 2-D, incompressible turbulent calculations of Moore, et al. showed an area of enhanced heat transfer on the pressure side of a turbine blade tip as shown in Fig. 39. The heat transfer was enhanced by up to 1.8 times the downstream fully developed value in the first two to three tip gap heights. The estimated intersection of the free streamline with the sidewall of $\frac{X_i}{W}$ between 0.4 and 1.4 observed in Fig. 36 would indicate a shock forming within this region of already enhanced heat transfer. The shock-boundary layer interaction could serve to further enhance the heat transfer. Increased heat transfer would lead to higher metal temperatures and larger losses of material. This would reduce both the efficiency and expected useful life of the turbine blade

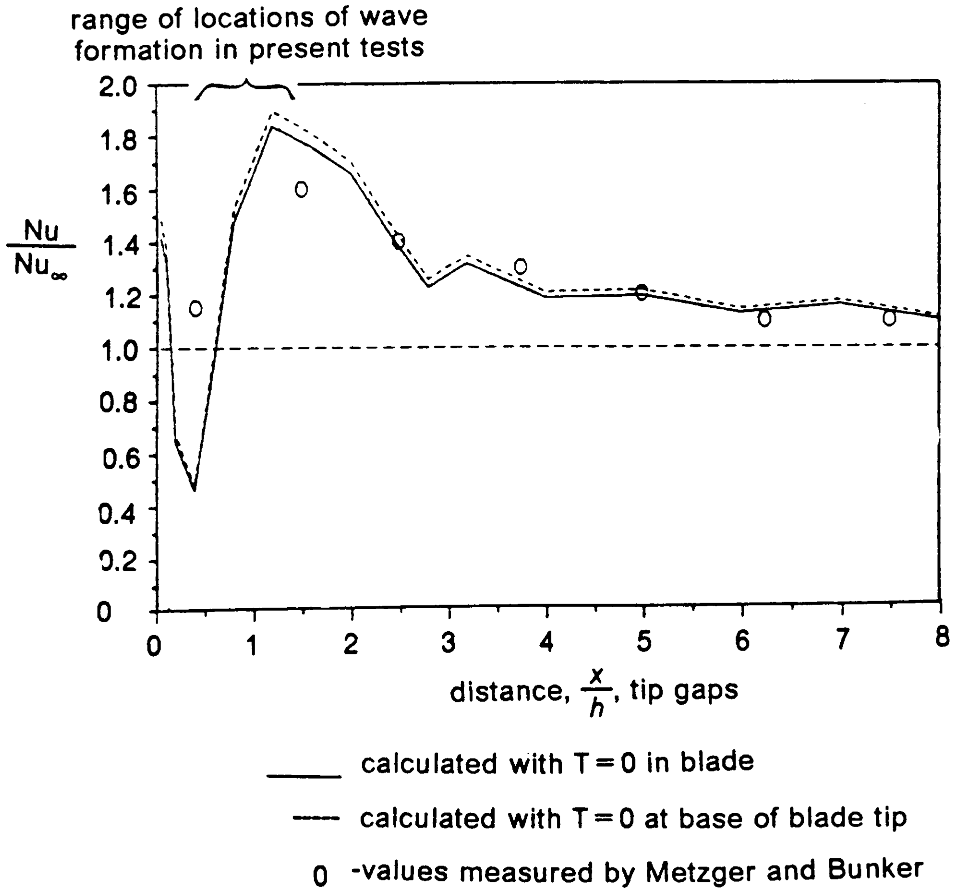

Figure 39. Enhanced heat transfer in a turbine blade tip gap

Chapter VI

Conclusions

Tests to study the formation mechanism of shocks in long orifices were performed to gain insight into the compressible flow in tip clearance gaps of turbomachinery blading. The flow was modeled with a sharp-edged rectangular channel on a water table. Tests were run with equivalent back pressure ratios, $\frac{P_b}{P_0}$, of about 0.038 and 0.181 on channels with aspect ratios (length to half-width, $\frac{l}{w}$) of 2.6 and 1.32. In addition, tests with the $l/w = 2.6$ channels were run with model scales of 2 and 0.769 of the basic model configuration.

At the back pressures used, the flow accelerated from subcritical ($F < 1$), expanding around the corner to critical ($F = 1$) and then remaining supercritical ($F > 1$) for the rest of the channel. Near the corner at the channel entrance, the flow exhibited a surface dimple, or area of low surface height and high local Froude number, due to overexpansion around the corner. Downstream of this region, an oblique wave was observed starting at the channel wall. In the present tests, the dimple Froude numbers ranged from 1.6 to 2.3. The measured angles of the waves relative to the channel sidewall were 37, 31, 31, 35, and 28 degrees compared with the theoretical angles of 40, 44, 45, 31, and 35 degrees, respectively, calculated theoretically using the measured surface heights.

The results observed on the water table suggest a model for the formation of the oblique hydraulic jump. As the flow enters the channel, it expands around the corner creating a region of minimum water height. The "free streamline" separates from the wall at the channel entrance; and, for F greater than about 1.18, it curves back to intersect the channel sidewall. At this point, the free stream flow is turned parallel to the sidewall, giving rise to an oblique hydraulic jump.

The above model was applied to compressible gas flows by comparing the test results to compressible sharp-edged orifice flow calculations found in the literature. Comparison was made between the lines of critical flow and sonic lines for both types of flow. The shapes of the critical flow lines agreed very well with the shapes of the sonic lines observed in the calculations in the literature.

The equivalent free stream turning angles calculated with the modified hydraulic analogy compared well with the values obtained from the compressible flow results in the literature. As the freestream Mach or Froude number increases, the angle of turn also increases. The test data gave angles of turn in the range of 13.5 degrees to 19.5 degrees; these were about 78 percent of the values suggested by the sharp-edged orifice calculations of Norwood.

The above findings all lend support to the basic flow model. This model was then used to predict a shock formation in the compressible flow near the inlet of a long orifice to show how such an event could occur in a turbine tip clearance gap. The presence of a shock in a tip gap would have two major implications: increased losses due to higher entropy generation, and possible higher heat transfer to the blade tip. Larger losses and higher blade tip temperatures would result in lower efficiencies and shorter useful blade life.

Chapter VII

REFERENCES

1. Rains, D.A., "Tip Clearance Flows in Axial Flow Compressors and Pumps," *California Institute of Technology, Hydrodynamics and Mechanical Engineering Laboratories, Report No. 5,* June, 1954.

2. Moore, J., and Tilton, J.S., "Tip Leakage Flow in a Linear Turbine Cascade," *Transactions of ASME, Journal of Turbomachinery,* vol. 110, pp 18-26, January, 1988

3. Graham, J.A.H., "Investigation of a Tip Clearance Cascade in a Water Analogy Rig," *ASME Paper No. 85-IGT-65,* 1985.

4. Bindon, J.P., "Flow Visualisation of Axial Turbine Tip Clearance Flow Using a Linear Cascade," *Eighth International Symposium on Air Breathing Engines,* AIAA, Cincinnati, pp436-444, June 14-19, 1987.

5. Moore, J., Moore, J.G., Henry, G.S., and Chaudhry, U., "Flow and Heat Transfer in Turbine Tip Gaps," *ASME Paper No. 88-GT-188,* 1988.

6. Henry, G.S., "A Study of Tip-Leakage Flow Through Orifice Investigations," *M.S. Thesis,* Virginia Polytechnic Institute and State University, Blacksburg, Virginia, October, 1987.

7. Page, L., *Introduction to Theoretical Physics,* D. Van Nostrand Company, Inc., New York, 1952.

8. Johnson, R.H., "The Hydraulic Analogy and Its Use with Time Varying Flows," *G.E. Research Laboratory Report No. 64-RL-(3755c),* August, 1964.

9. Laitone, E.V., "A Study of Transonic Gas Dynamics by the Hydraulic Analogy," *Journal of the Aeronautical Sciences,* April, pp 265-272, 1952.

10. Ippen, A.T., and Harleman, D.R.F., "Certain Quantitative Results of the Hydraulic Analogy to Supersonic Flow," *Ohio Engineering Station Bulletin #149--Proceedings of the 2nd Midwestern Conference on Fluid Mechanics,* 1952.

11. Benson, R.S., and Pool, D.E., "Compressible Flow Through a Two-Dimensional Slit," *Int. J. Mech. Sci.,* vol. 7, pp 315-336, 1965.

12. Norwood, R.E., "Two Dimensional Transonic Gas Jets," *Sc. D. Thesis,* Massachusetts Institute of Technology, Cambridge, Massachusetts, June, 1961.

13. Ippen, A.T., "Mechanics of Supercritical Flow," *Classic Papers in Hydraulics,* ASCE, New York, 1982.

14. Ippen, A.T., and Harleman, D.R.F., "Verification of Theory for Oblique Standing Waves," *Transactions of the ASCE,* vol. 121, pp 678-694, 1956.

15. Schreier, S., *Compressible Flow,* John Wiley and Sons, New York, 1982.

Appendix A

Development of Oblique Hydraulic Jump/Shock Relations

Oblique hydraulic jumps

Ippen [13,14] provides development and experimental verification of the theory for oblique waves or hydraulic jumps. This theory is partially developed here for water flow undergoing an abrupt change in flow direction as shown in Fig. A1.

Continuity applied per unit length into the page yields

$$h_1 V_{1n} = h_2 V_{2n} \tag{1}$$

where

$$V_{1n} = V_1 \sin \beta$$

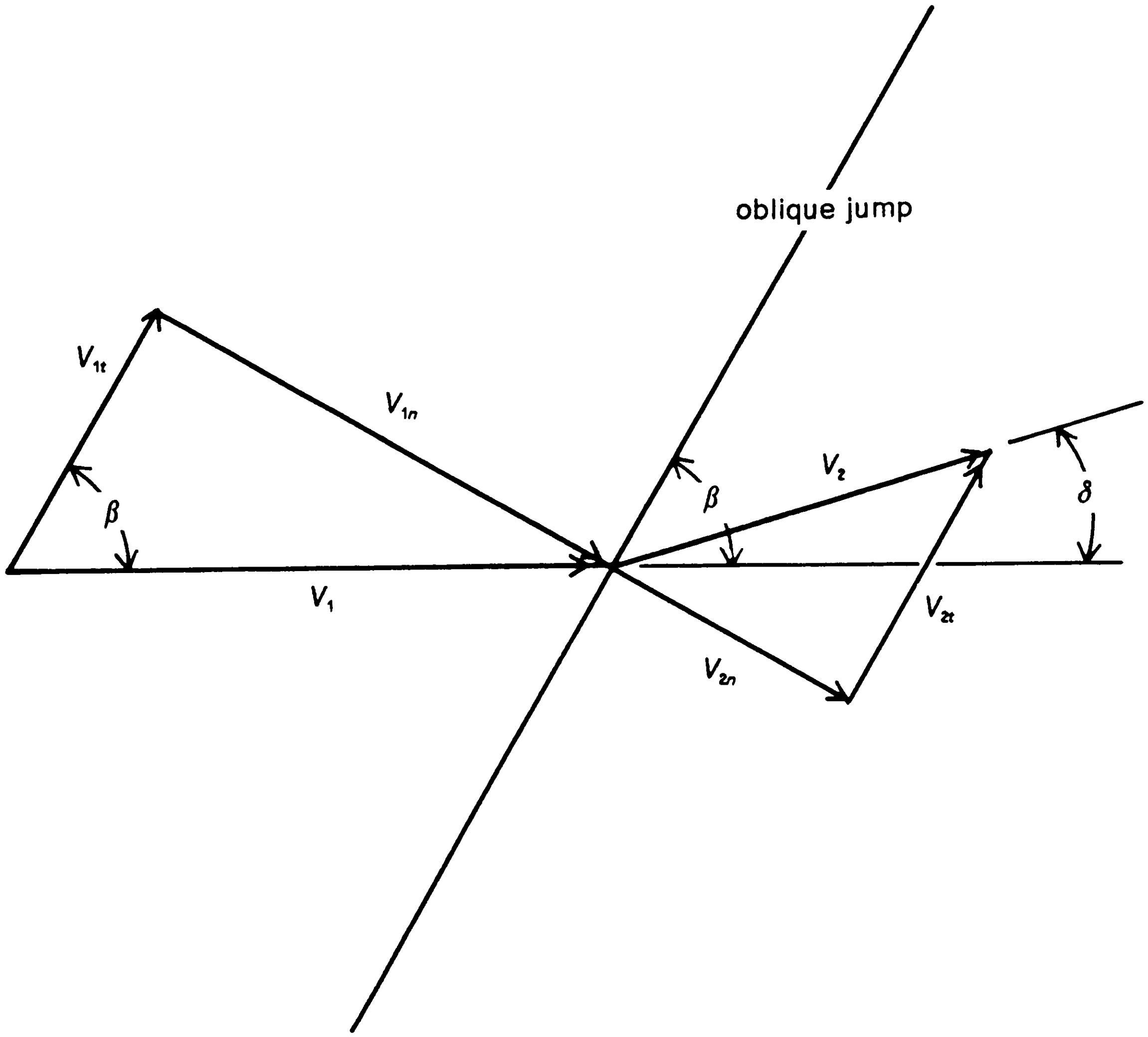

Figure A1. Flow undergoing an oblique hydraulic jump

$$V_{2n} = V_2 \sin(\beta - \delta) \ .$$

Next, momentum is applied in the tangential direction resulting in

$$V_{1t} = V_{2t}$$

where

$$V_{1t} = V_1 \cos \beta$$

$$V_{2t} = V_2 \cos(\beta - \delta) \ .$$

Applying momentum in the normal direction yields

$$V_{1n}^2 h_1 + \frac{g h_1^2}{2} = V_{2n}^2 h_2 + \frac{g h_2^2}{2} \ .$$

Substituting $V_{2n} = V_{1n} \dfrac{h_1}{h_2}$ from equation 1 and solving for V_{1n} gives

$$V_{1n}^2 = \frac{g h_1}{2} \frac{h_2}{h_1} \left(\frac{h_2}{h_1} + 1 \right) \ .$$

Substituting for V_{1n} and solving for β,

$$\sin \beta = \frac{\sqrt{g h_1}}{V_1} \sqrt{\frac{1}{2} \frac{h_2}{h_1} \left(\frac{h_2}{h_1} + 1 \right)} \ .$$

The inlet Froude number $F_1 = \dfrac{V_1}{\sqrt{g h_1}}$ so

$$\sin \beta = \frac{1}{F_1} \sqrt{\frac{1}{2} \frac{h_2}{h_1} \left(\frac{h_2}{h_1} + 1 \right)} \ . \qquad (2)$$

Equation 1 can be rearranged to give

$$\frac{h_2}{h_1} = \frac{V_{1n}}{V_{2n}} = \frac{V_1 \sin\beta}{V_2 \sin(\beta - \delta)} \quad .$$

Letting $V_1 = \frac{V_{1t}}{\cos\beta}$, and $V_2 = \frac{V_{2t}}{\cos(\beta - \delta)}$,

$$\frac{h_2}{h_1} = \frac{\tan\beta}{\tan(\beta - \delta)} \quad . \tag{3}$$

Solving equation 2 for $\frac{h_2}{h_1}$ yields

$$\frac{h_2}{h_1} = \frac{1}{2}\left(\sqrt{1 + 8F_1^2 \sin^2\beta} - 1\right) \; . \tag{4}$$

If equations 3 and 4 are set equal and solved for tan δ,

$$\tan\delta = \frac{\tan\beta\left(\sqrt{1 + 8F_1^2 \sin^2\beta} - 3\right)}{2\tan^2\beta + \sqrt{1 + 8F_1^2 \sin^2\beta} - 1} \quad . \tag{5}$$

A plot of equation 5 appears in Fig. A2 as the jump angle β against inlet Froude number F_1 for various turning angles, δ.

Oblique shock waves

Equations similar to those for oblique hydraulic jumps can be developed for oblique shock waves. Consider flow across an oblique shock as shown in Fig. A3.

Applying continuity yields

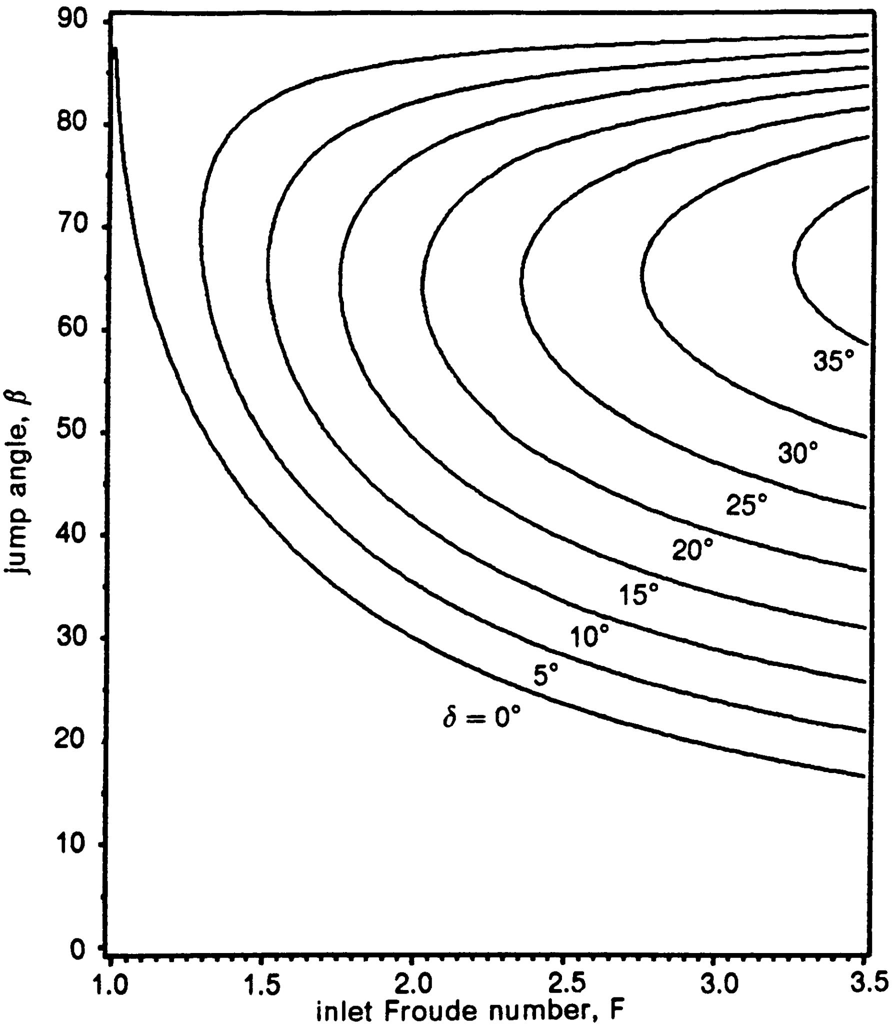

Figure A2. Oblique hydraulic jump angle as a function of F and turning angle

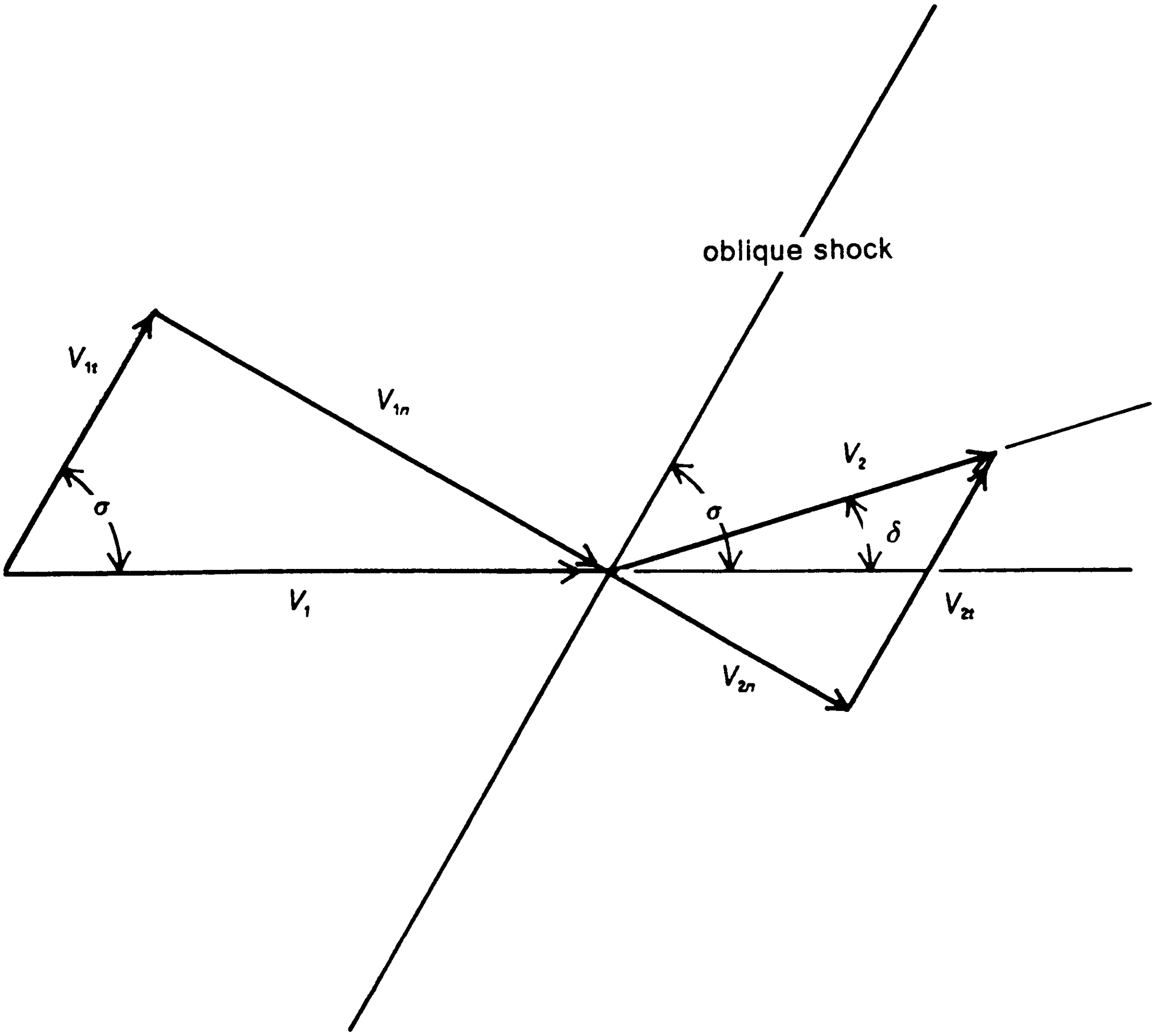

Figure A3. Flow past an oblique shock

$$\rho_1 V_{1n} = \rho_2 V_{2n} \tag{6}$$

where

$$V_{1n} = V_1 \sin \sigma$$

and

$$V_{2n} = V_2 \sin(\sigma - \delta) \ .$$

Momentum in the tangential direction will yield

$$V_{1t} = V_{2t}$$

and in the normal direction gives

$$P_1 + \rho_1 V_{1n}^2 = P_2 + \rho_2 V_{2n}^2 \ .$$

Rearranging equation 6 results in

$$\frac{\rho_2}{\rho_1} = \frac{V_{1n}}{V_{2n}} = \frac{V_1 \sin \sigma}{V_2 \sin(\sigma - \delta)} \ .$$

Letting $V_1 = \frac{V_{1t}}{\cos \sigma}$ and $V_2 = \frac{V_{2t}}{\cos(\sigma - \delta)}$,

$$\frac{\rho_2}{\rho_1} = \frac{\tan \sigma}{\tan(\sigma - \delta)} \ . \tag{7}$$

Schreier [15] gives the density ratio across an oblique shock as

$$\frac{\rho_2}{\rho_1} = \frac{\frac{k+1}{2} M_1^2 \sin^2\sigma}{1 + \frac{k-1}{2} M_1^2 \sin^2\sigma} \quad . \tag{8}$$

Setting equations 7 and 8 equal and solving for tan δ yields

$$\tan \delta = \frac{\left(M_1^2 \sin^2\sigma - 1\right) \cot \sigma}{\frac{k+1}{2} M_1^2 - M_1^2 \sin^2\sigma + 1} \quad .$$

This equation is plotted in Fig. A4 as σ versus M_1 for various values of δ.

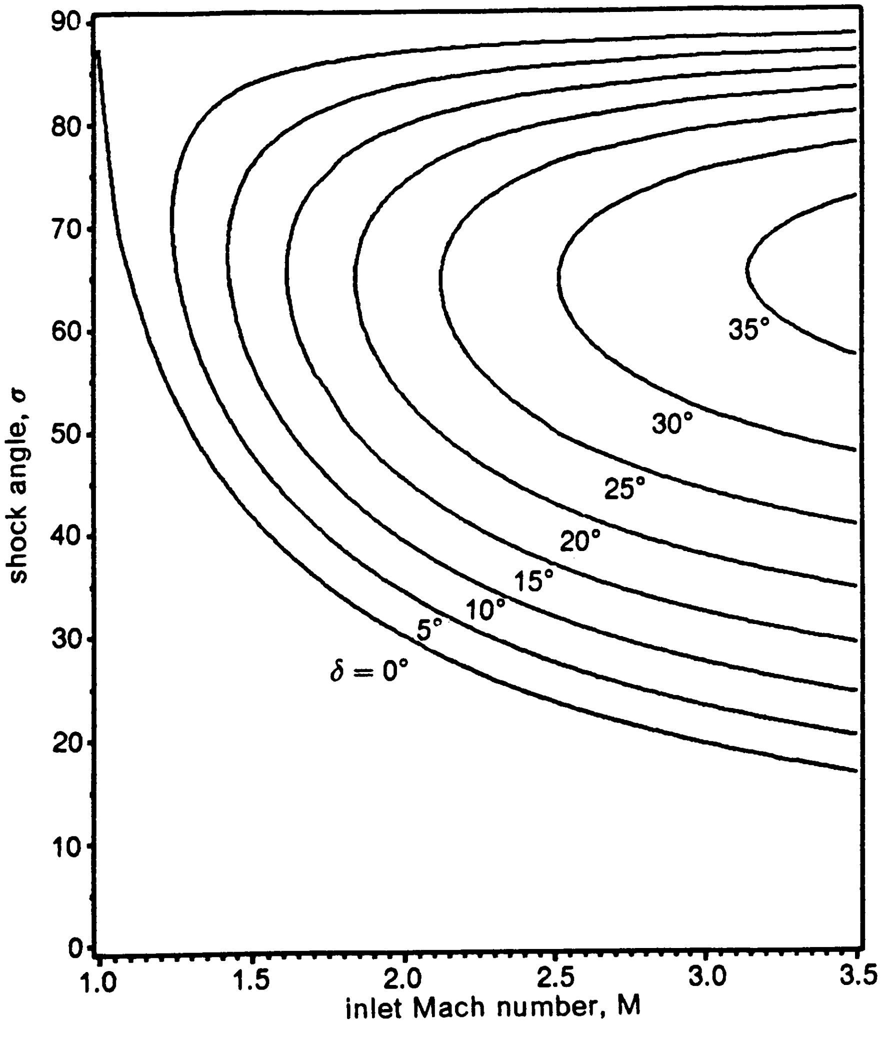

Figure A4. Shock angle as a function of Mach number and deflection angle

Appendix B

Determination of Surface Tension

The surface tension of the water was found by measuring the rise of a column of water in a capillary tube. Figure B1 shows a sketch of the experimental setup for this method. The capillary tube is thrust into the filled beaker and raised slightly before being clamped in place. The distance h from the water surface to the bottom of the meniscus is then measured.

The surface tension can be determined by considering that the surface tension, acting on the circumferential surface of the meniscus, supports the weight of the column of water below the meniscus.

$$2\pi r T = \pi r^2 \rho g h \qquad (1)$$

where r is the radius of the circle of contact of the meniscus (radius of the capillary tube), and T is the surface tension. Thus

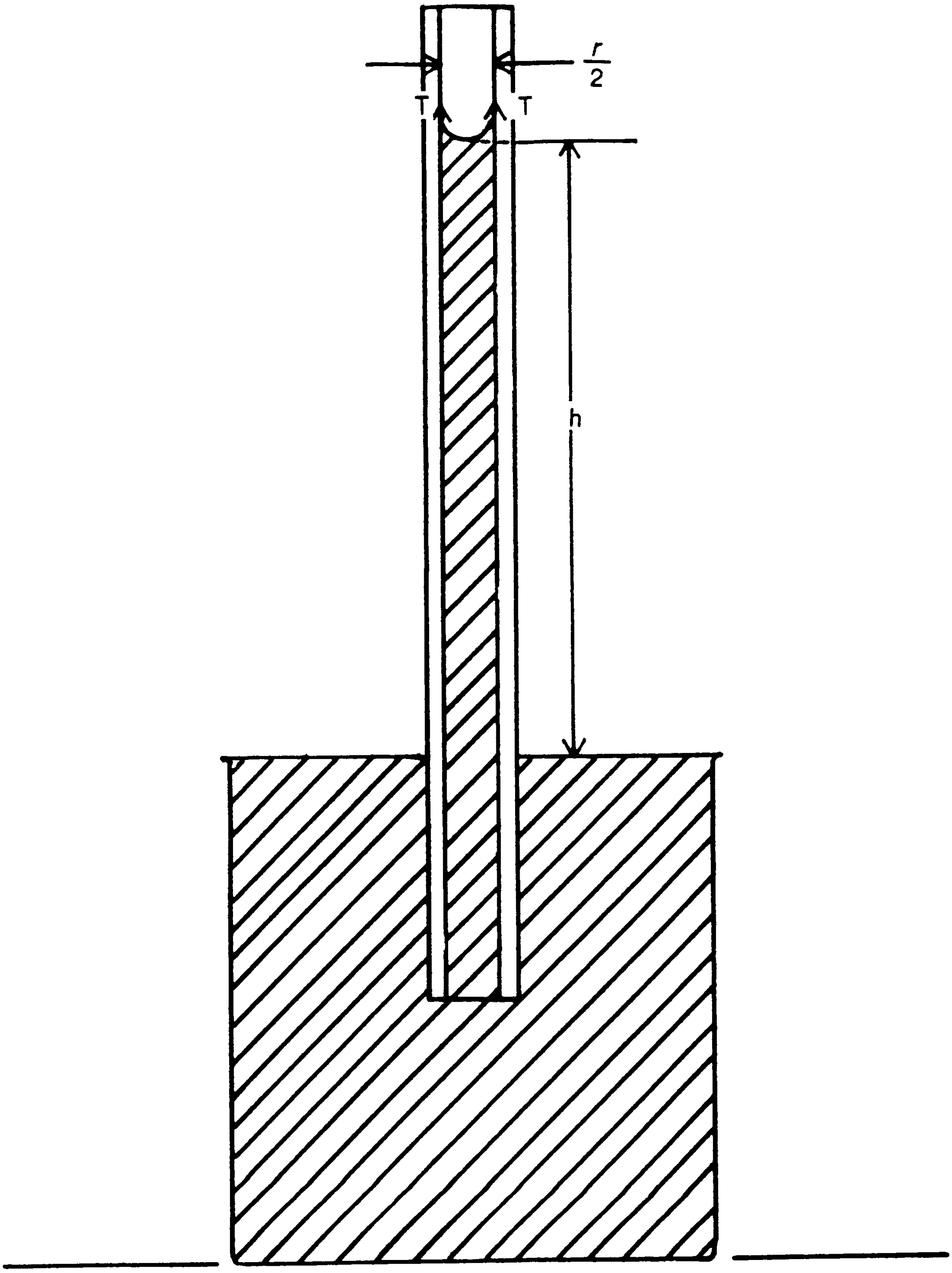

Figure B1. Surface tension measurement apparatus

$$T = \frac{\rho g h r}{2}$$

Assuming that the surface of the meniscus is hemispherical, the weight of the water above the bottom of the meniscus will be

$$\left(\pi r^3 - \frac{2}{3}\pi r^3\right)\rho g = \frac{1}{3}\pi r^3 \rho g$$

Since the surface tension must also act to support this liquid, equation 1 can be more accurately written as

$$2\pi r T = \pi r^2 \rho g h + \frac{1}{3}\pi r^3 \rho g$$

or

$$T = \frac{1}{2}\rho g r\left(h + \frac{r}{3}\right).$$

Thus by using a capillary tube of known radius, and measuring the height of the column of liquid in the tube, the surface tension can be calculated.

In the present measurements a glass capillary tube of 1.3 mm inside diameter was used, and the water rose heights h in the range of 7.87 to 21.8 mm. The heights were measured with a machinists scale with an accuracy of ± 0.25 mm. The scale was held in place with a clamp. Thus the accuracy of determination of the surface tension was ± 3 percent.

Appendix C

Analysis of Possible Errors in Locating the F=1 Line

The errors in locating the line of critical flow come mainly from two possible sources: locating the point of the surface probe and slight fluctuations of the water depth in the flow. Due to the wobble in the surface probe, its location is known only to within 0.03 in (0.076 cm). Based on the half-width of the channel, w, this represents an error, $\frac{\Delta x}{w}$, of ± 0.02 for case B, ± 0.01 for cases A, D, and E, and ± 0.025 for case C.

Slight fluctuations in the depth of the flow can lead to error in locating the F = 1 line. During the course of the tests, these fluctuations were on the order of $\delta h = 0.025$ cm. An estimate of the error in locating the F = 1 line can be found by

$$\frac{\Delta x}{w} \simeq \frac{\delta h}{\frac{dh}{dx} w}$$

where $\frac{dh}{dx}$ is the slope of the water surface in the direction of flow along the centerline. This can be approximated by $\frac{\Delta h}{\Delta x}$, where Δh is the change in water height observed over the distance Δx in the data. Doing so gives $\frac{\Delta x}{w}$ of ± 0.04 for cases A, C, and E, and ± 0.03 for cases B and D. Adding these errors to those resulting from the pointer location results in Δx of $\pm 0.047w$ for cases A and E, $\pm 0.05w$ for case B, $\pm 0.065w$ for case C, and $\pm 0.043w$ for case D. Thus the error in locating the $F=1$ line is on the order of $\pm 0.05w$.